The geochemical consequences of mixing melts from a heterogeneous mantle

John F. Rudge[a,*], John Maclennan[b], Andreas Stracke[c]

[a]*Bullard Laboratories, Department of Earth Sciences, University of Cambridge, Madingley Road, Cambridge, CB3 0EZ, UK.*
[b]*Department of Earth Sciences, University of Cambridge, Downing Street, Cambridge, CB2 3EQ, UK.*
[c]*Westfälische Wilhelms Universität, Institut für Mineralogie, 48149 Münster, Germany.*

Abstract

Binary mixing is one of the most common ways of describing the relationships between incompatible element concentrations and Sr-Nd-Pb isotopic ratios in oceanic basalts. Apparent binary mixing trends are seen in a wide variety of data sets, both at a local-scale and globally. Here we focus on data from Iceland where isotopic variations in whole-rock samples and olivine-hosted melt inclusions demonstrate the presence of high-amplitude, short length-scale mantle heterogeneity. Binary mixing models fail to provide an adequate fit to data for moderately incompatible and compatible elements, which provides evidence that some of the variation in melt compositions arises from the fractional melting process itself. To explore the role of mixing in determining the geochemical systematics of oceanic basalts we have developed a new model of the mixing of fractional melts from a bi-lithological mantle source where small enriched fusible heterogeneities are embedded in a refractory depleted matrix. This model is a statistical model, based on the Dirichlet distribution, that allows us to determine the expected statistical distributions of melt compositions. The Icelandic data appears to provide evidence that the mixing process is not uniform with depth, and that the deepest melts appear to have undergone a greater degree of homogenisation than the shallower melts. The model most closely resembles the data when all melts beneath a depth corresponding to $\sim$5% melting of the refractory lithology are homogenised. We speculate that this depth marks the transition between diffuse and channelised melt flow. This new statistical model of mixing challenges some of the conventional interpretations of trace element-isotope systematics. Notably, picking mantle end-members from apparent binary mixing arrays in isotope ratio plots is fraught with difficulty: in our models the apparent binary mixing arrays do not point towards the isotopic compositions of their mantle sources (with the exception of Pb-Pb).

1. Introduction

Isotopic and trace element data from Mid-Ocean Ridge Basalt (MORB) and Ocean Island Basalt (OIB) samples are often interpreted in terms of binary mixing between two homogeneous materials. On the scale of individual ridge segments or ocean island volcanoes

---

*Corresponding author. Email: rudge@esc.cam.ac.uk. Tel: +44-1223-765545. Fax: +44-1223-360779.

such binary mixing models often provide good fits to the observed isotopic and incompatible trace element ratios (Abouchami et al., 2000, 2005; Tanaka et al., 2008; Blichert-Toft and Albarède, 2009; Hanano et al., 2010; Stracke et al., 2003b; Peate et al., 2009; Stracke et al., 1999). It has long been recognised that the end-members of these binary mixing arrays need not correspond to globally significant mantle components, and that mixing of three components can lead to pseudo-binary mixing arrays when two of the components mix fully before mixing with a third component (Hamelin et al., 1986; Douglass and Schilling, 2000). Such regional-scale mixing is, however, consistent with the widely accepted assumption that the isotopic compositions of the end-members of mixing arrays, or even the individual samples themselves, correspond to those of substantial masses of mantle underneath oceanic volcanoes. This approach has arisen naturally from a view of the mantle where short-lengthscale isotopic and mineralogical variations are unimportant. Melts from such a mantle would have an isotopic composition identical to that of large volumes of the solid from which they are produced.

The study of small-scale variation in the compositions of the melts and mantle residues generated at spreading ridges has highlighted the importance of the melting process as an additional generator of geochemical diversity. The observation of substantial variation in the incompatible trace element contents and trace element ratios of olivine-hosted melt inclusions in individual MORB samples was accounted for by a model involving generation of extreme compositional variation during fractional melting (Sobolev and Shimizu, 1993). A similar model was used to account for the observation of residual clinopyroxene with depleted incompatible trace element contents in abyssal peridotites (Johnson et al., 1990). These models are consistent with a range of compositional and physical arguments for the separation of melts from the mantle at low porosities followed by rapid channelised flow towards the surface (McKenzie, 1985; Kelemen et al., 1997). The observations of extreme small-lengthscale variation in the trace element compositional record of mantle melts were believed to demonstrate that near-fractional melting was the primary cause of local-scale trace element variation, and provided evidence that the average trace element compositions of oceanic basalts is different from those of their mantle source regions (Sobolev and Shimizu, 1993; Johnson et al., 1990). These differences between melt and source extended even to the incompatible trace element ratios (Hofmann et al., 1986). A number of workers produced models of fractional melting of a single homogeneous mantle source composition, demonstrating the substantial range of trace element compositions that can be generated without any variation in the isotopic composition of the basalts (Gast, 1968; Shaw, 1970; Slater et al., 2001; Maclennan et al., 2003b). Since these models did not involve the generation of isotopic variability, they provided no challenge to the assumption that MORB and OIB isotopic arrays could be used to identify the compositions of solid material in the mantle rising under oceanic volcanoes.

More recent studies (Stracke et al., 2003b; Stracke and Bourdon, 2009; Peate et al., 2009; Cordier et al., 2010; Waters et al., 2011) have looked at a combination of trace element, major element, and isotopic data using samples from localities tightly constrained in space and time. These studies have found strong correlations in whole rock data between trace element ratios and isotopic ratios. Melt inclusion studies (Maclennan, 2008b) echo these strong correlations, at least for incompatible trace element concentrations and isotopes. The correlations suggest that heterogeneity in the mantle source has a key control on the observed trace element heterogeneity. Nevertheless, some part of the observed trace element heterogeneity must

be generated by the melting process itself, as reflected in the systematics of REE variation in olivine-hosted melt inclusions (Maclennan et al., 2003a). Furthermore, the presence of U-series disequilibrium in young basalts from Iceland demonstrate that highly incompatible elements can be fractionated from each other by the melting process (Condomines et al., 1981; Hémond et al., 1993; Stracke et al., 2003c; Kokfelt et al., 2006; Koornneef et al., 2012a).

A further complication to understanding the isotopic systematics of oceanic basalts is that isotopic heterogeneity may be coupled with lithological heterogeneity and hence with fusibility (Hirschmann and Stolper, 1996; Stracke et al., 1999; Phipps Morgan, 2001; Stracke et al., 2003b,c; Katz and Rudge, 2011; Shorttle and Maclennan, 2011). For example, recycled crustal material, which is often thought to be the carrier of the isotopically enriched signature, may be more pyroxenitic and thus more fusible than the rest of the depleted peridotitic mantle. The isotopic composition of a sample formed by melting of a multi-lithology source will be biased from that of the mean mantle source, and will be a function of the degree of melting. As a result, a number of studies have explained the correlations between isotopes and trace elements as arising naturally from varying degrees of melting of a lithologically heterogeneous source (Phipps Morgan, 1999; Ito and Mahoney, 2005a,b; Stracke and Bourdon, 2009; Ingle et al., 2010).

The present manuscript seeks to address the following key question: Why do binary mixing models work so well if the generation of melt in the mantle is dominated by fractional melting? This question becomes even more pressing when it is understood that fractional melting of a heterogeneous mantle can fill a huge volume in isotope and trace-element compositional space. We believe the answer lies in understanding precisely how the fractional melts are mixed to form the samples we see at the surface. To this end we have developed a new model of melting and the mixing of melts from a bi-lithological source, building on the previous studies by Stracke and Bourdon (2009) and Maclennan (2008b). The manuscript is organised as follows: the next section describes the main observational constraints, and is followed by a description of a new statistical model. Subsequent sections discuss the application of the model to trace element and isotopic data for whole rocks and melt inclusions. Detailed mathematical derivations are provided in an appendix at the end of the manuscript.

The data used in the examples throughout this manuscript come from Iceland, but the modelling techniques and ideas we develop are relevant for understanding melt mixing more generally. Iceland provides one of the best windows into the melt mixing process: On Iceland it is possible to constrain the origin of basalts tightly in space and time; spatially because it is possible to make detailed maps of volcanic flows in the field; and temporally because one can distinguish easily between subglacial and postglacial eruptions through their geomorphology, and use tephrochronology to bracket the ages of postglacial flows (Sæmundsson, 1991). There is a large quantity of high quality data available from Iceland which has a wide spread of different geochemical measurements (majors, traces, and isotopes) made on exactly the same set of samples, both whole-rock samples and olivine-hosted melt inclusions. Having all the measurements on the same samples is particularly important for understanding melt mixing because of the information it provides on the correlations between different observables.

2. Observations

2.1. Isotope – trace element systematics

2.1.1. Apparent Binary Mixing

[Figure 1 about here.]

Detailed studies of geochemical variations of the eruptive products of individual volcanic systems on spreading ridges or ocean islands on the timescale of 10^3–10^5 years have revealed well-defined correlations between isotope ratios of incompatible elements, most commonly Sr, Nd and Pb. Isotope-isotope plots have been interpreted by many authors in terms of binary mixing between two end-member solids or two end-member melts. These interpretations have been supported by the strong correlation of these isotope ratios not only with incompatible trace element ratios (e.g. Nb/Y) but also with elemental concentrations in primitive basalts, such as La and Nb (Zindler et al., 1984; Stracke et al., 1999; McKenzie et al., 2004; Cordier et al., 2010; Waters et al., 2011). For example, the relationship between the isotope ratio $^{208}Pb/^{206}Pb$ and both the Nb concentration and the La/Yb ratio of primitive olivine-hosted melt inclusions and whole-rock samples from the Reykjanes Peninsula in Iceland were shown by Maclennan (2008b) to be well matched by binary mixing between the extreme end-member melt compositions (Figure 1A,C).

[Figure 2 about here.]

Further evidence for the apparent success of binary mixing can be observed in the whole-rock data from the Theistareykir volcanic system plotted in Figure 2 (Stracke et al., 2003b; Slater et al., 2001). These Theistareykir samples are collected from a region ∼30 km in extent and are all from postglacial lava flows, less than ∼12 kyr old. The samples stretch along linear arrays on these plots of incompatible trace element and isotope ratios, with modest scatter partly reflecting uncertainty in the analyses. The Reykjanes Peninsula samples are from a slightly larger region, ∼50 km long, with the filled symbols in Figure 2 being postglacial samples. Samples from the last glaciation have compositions that either sit in the same range as postglacial samples or extend the arrays at the enriched end. On first inspection the Reykjanes whole-rock samples also appear to stretch along binary mixing arrays. Indeed, Thirlwall et al. (2004) has highlighted that the Sr-Nd-Pb isotopes systematics of localised sets of samples in Iceland are extremely well matched by binary mixing arrays, with the misfit of such binary mixing curves to the data being similar to the analytical uncertainty. This realisation lead Thirlwall et al. (2004) to suggest that mixing between a relatively small number of mantle components may account for the full range of isotopic variation seen on Iceland. They used plots such as Figure 2C to estimate the composition of mantle components under Iceland and their preferred compositions are shown as crosses on Figure 2C.

2.1.2. Breakdown of Binary Mixing

While many aspects of isotope-trace element systematics in localised sample suites can be accounted for by binary mixing, several key features of the data cannot be matched by such simple models. In the Reykjanes Peninsula data, there is significant scatter of the data away from binary mixing lines and Thirlwall et al. (2004) suggested that a third component was required to account for this spread. Such scatter away from binary mixing lines is a

4

feature of many OIB and MORB sample suites. An alternative cause of scatter on plots such as Figure 2C will be described later in this paper.

Further evidence for the breakdown of binary mixing models can be obtained by inspection of Figure 1. The weaker correlations observed between isotope ratios and the concentrations of more compatible elements, such as Yb or Y, or their ratios, such as Sm/Yb, do not conform to simple binary mixing relationships (Figure 1B,D). This observation might be interpreted as an indication that more than two melt compositions are supplied from the mantle to the plumbing system of individual volcanoes. However, the poor resemblance to a binary mixing model results, in part, from the overprinting effect of fractional crystallisation on Yb and Y concentrations. Suites of melt inclusions hosted in forsteritic olivines may have variations of > 100 in the concentrations of some of the most incompatible elements such as Nb, while less compatible elements such as Y vary by a factor of ~ 5. This difference in the range of highly and moderately incompatible elements is predicted for instantaneous fractional melt compositions of the mantle. The relatively modest variation in the Y concentration of mantle melts allows later processes, such as fractional crystallisation, to add significant noise to the mantle signal. A factor of 4 variation in Y is observed at nearly constant $^{208}Pb/^{206}Pb$ in olivine-hosted melt inclusions from the Reykjanes Peninsula, but this variation is greater than can be produced by fractional crystallisation alone. A factor of 4 in Y requires approximately 75% crystallisation, whereas the limited range of forsterite contents of the host olivines (Fo_{84-91}) are expected to be generated during the first 40% of crystallisation of Icelandic mantle melts (Maclennan et al., 2003a). Therefore, part of the range of Y at fixed $^{208}Pb/^{206}Pb$ must reflect variation in mantle melts.

Furthermore, the scatter observed in Sm/Yb at constant $^{208}Pb/^{206}Pb$ in Figure 1D is unlikely to result from fractional crystallisation and indicates that mantle melts with variable Sm/Yb are associated with the enriched $^{208}Pb/^{206}Pb$ isotopic composition. If this interpretation is correct, then binary mixing of two melts cannot account for the observations presented in Figure 1. An important concern in the interpretation of basaltic geochemistry from Iceland and elsewhere is that cross-plots of isotope ratios and highly incompatible element ratios are often understood in terms of simple binary mixing. However, examination of the relationships of moderately incompatible elements reveals more complex behaviour, which means that the simplest interpretation of the isotope ratio plots may be misleading.

2.2. Forsterite content – trace element systematics

Additional evidence against the binary mixing model is provided by the relationship between the trace element variation of melt inclusions and their olivine hosts. The details of this relationship were first noted by Maclennan et al. (2003a) in a study of olivine-hosted melt inclusions from the Borgarhraun lava flow and used as evidence to support the origin of trace element variation in the melt inclusions from mixing of a range of instantaneous fractional melt compositions, as explained below.

[Figure 3 about here.]

Mixing between the melt inclusions with extreme La/Yb from Borgarhraun generate a steep array on Figure 3 which plots La against Yb. The field of melt compositions that can be generated by fractional crystallisation of the inclusions with extreme La/Yb is smaller than

the observed range of compositions, indicating that processes in addition to binary mixing of two mantle melts and fractional crystallisation are occurring.

[Figure 4 about here.]

Figure 4 plots La and Yb as a function of the composition of their olivine hosts. As noted by Maclennan et al. (2003a), the pattern of variation of La concentration with the forsterite content of the host olivines is different to that of Yb, and this cannot be explained by binary mixing (see Appendix A). In Figure 4A,B it can be seen that the mean La concentration of the melt inclusions increases with decreasing forsterite content of the olivine host, and that the variance in La of the inclusions remains elevated between Fo_{91} and Fo_{88}, with a peak close to Fo_{88}. In contrast, Figure 4C,D show that mean Yb concentrations fall with decreasing forsterite content between Fo_{91} and Fo_{85}, and that the variance in Yb exhibits a strong peak at Fo_{90} and then falls with decreasing forsterite content.

This decoupling of the behaviour of La and Yb is not expected from simple models of fractional crystallisation, because during the initial stages of cooling and crystallisation of mantle melts both La and Yb are expected to be incompatible and to exhibit coupled variations in their concentration in the melt. However, the characteristic decoupling of the variation of La and Yb as shown in Figure 4 can be accounted for by mixing of instantaneous fractional melts from a melting column of a single source (Maclennan et al., 2003a). Instantaneous fractional melts can generate the required pattern of primary melt compositions to account for the decoupling due to the differing compatibility of La and Yb during melting in the presence of garnet. Furthermore, the fact that the forsterite content of the olivines that would crystallise from the instantaneous fractional melts drops during the progression of decompression melting allows the melting process to account for the decoupling of La and Yb across the olivine compositional interval from Fo_{88} to Fo_{92}.

[Figure 5 about here.]

At the onset of melting in the garnet field, La is incompatible and Yb has a partition coefficient close to 1. Therefore, the first melts have the highest La of any predicted melts and are in equilibrium with the least forsteritic olivine, Fo_{85}, of any of the predicted melts (Figure 5). However, the Yb content of these first melts is not extreme, due to the presence of garnet. The Yb composition of these first melts is labelled as point 1 on the dashed curve in Figure 5. As melting proceeds, the La content of the instantaneous fractional melts drops monotonically towards zero, and the forsterite content of the equilibrium olivines rises towards Fo_{92}. The behaviour of Yb is more complicated. At point 2 on the dashed curve in Figure 5 the Yb concentration starts to rise, corresponding to the arrival of spinel as a residual phase in the melting mantle at decreasing depth. Between point 1 and point 2 garnet is the stable aluminous phase in the peridotite, while between point 2 and 3 both garnet and spinel are present. The peak Yb concentration, at point 3, corresponds to the disappearance of garnet from the residue and where Yb becomes highly incompatible. The drop in Yb contents between points 3 and 4 corresponds to increasing extents of melting of spinel peridotite.

One crucial observation from Figure 5 is that, in mantle melts, the full range of variation in Yb is established in melts that are in equilibrium with olivines between Fo_{92} and Fo_{90}, while mantle melts with extreme La contents are in equilibrium with Fo_{92} and Fo_{85}. Therefore, at forsterite contents greater than Fo_{90} mantle melting can contribute to variation in both Yb and La. Between Fo_{90} and Fo_{85} the mantle melts only add to variation in La and not in Yb. This difference in the behaviour of La and Yb during fractional melting of the mantle can therefore account for the observed difference in the evolution of the standard deviation of La and Yb with the host olivine composition (Figure 4). Addition of deep melts with extreme La can maintain variance in La in melt inclusions trapped in olivines between Fo_{90} and Fo_{88}. However, the intermediate Yb contents of these deep melts provide insufficient variation to counter the ineluctable progression of concurrent mixing and crystallisation and therefore the observed variance in Yb drops rapidly between Fo_{90} and Fo_{88}.

While the models of mixing of instantaneous fractional melts from Maclennan et al. (2003a) can account for the decoupling of Yb and La variations in forsteritic olivine, these models are based on melting of a single source so cannot account for the observed relationship between the isotopic and trace element variation present in Icelandic whole-rock and melt inclusion datasets (Figure 1). It is therefore necessary to demonstrate that models of melting of a compositionally heterogeneous source are also able to account for the observations presented in Figure 4.

3. A statistical model of melt generation and mixing

Whilst the isotopic variation in the Icelandic datasets indicates that high-amplitude and short lengthscale variation is present in the mantle source regions that contribute to individual volcanic systems, the melting process will also impart substantial compositional variability in the melts. This combination of source heterogeneity and fractional melting has the capacity to generate melts that fill a large compositional space and should not necessarily create strong correlations between elemental concentrations or ratios and isotope ratios. It is therefore necessary to develop a model of melt generation and mixing that can account not only for the apparent binary mixing relationships in incompatible element concentrations and ratios but also for the decoupling of elements of varying compatibility.

The new statistical model introduced in this work consists of two key components: a melting model and a mixing scheme. The melting model determines the compositions of the fractional melts; the mixing scheme determines how the fractional melts are mixed together to produce the samples.

3.1. Melting model

We consider the melting of a two-lithology source consisting of peridotite and pyroxenite. The details of the choice of the composition of these lithologies do not strongly influence the most general conclusions regarding the importance of mixing of fractional melts from a heterogeneous mantle. The behaviours that we highlight are, however, dependent on the presence of trace element and isotopic heterogeneity in the mantle that is correlated to variation in the melting behaviour of the material. In order to aid the comparison of our model results with observations with Iceland, however, we choose mantle lithologies that are similar to those that have been suggested to be melting under the island.

7

3.1.1. Nature of lithological heterogeneities

The peridotite composition is that estimated for depleted upper mantle, DMM, by Salters and Stracke (2004). Models were also run using the DMM composition of Workman and Hart (2005) in order to verify that the conclusions later drawn from the melting models are robust to variations in the details of the source compositions used. This DMM peridotite is more refractory and incompatible element depleted than the material chosen as the second lithology, which we refer to here as pyroxenite. The major element composition of this pyroxenite is set to that of the experimental material KG2, which was created by Kogiso et al. (1998) by mixing pyrolitic peridotite and average MORB compositions in 2:1 proportions. In detail, this composition lies just outside the pyroxenite field of Streckeisen (1976), but has a much higher pyroxene content than typical depleted mantle. It has recently been demonstrated that experimental batch melts of KG2 at pressures of 3 GPa have a similar major element composition to Icelandic basalts with enriched trace element and isotopic signatures (Shorttle and Maclennan, 2011). The trace element composition of the enriched source was set by mixing the depleted upper mantle composition of Salters and Stracke (2004) with the recycled MORB composition of Stracke et al. (2003a) in a 2:1 ratio, with the exception of the Pb concentration, which was set to 0.4 ppm.

While the geometry of the lithological heterogeneity is not directly specified in the models, it is assumed that there is no solid-state chemical interaction between the pyroxenite and the peridotite but that thermal equilibrium is maintained. This regime operates when the heterogeneities have a width within the range of 10s to 100s of metres (Sleep, 1984; Phipps Morgan, 2001; Kogiso et al., 2004; Katz and Rudge, 2011). These assumptions simplify the modelling of melt generation by adiabatic decompression of a lithologically variable mantle because both lithologies are melting along the same pressure-temperature path. In order to approximately match the mean composition of melts and the mean crustal thickness from the Theistareykir segment of northern Iceland (Maclennan et al., 2001b), and the major element constraints on the proportion of recycled basalt within the source regions of this segment (Shorttle and Maclennan, 2011), we set the DMM peridotite to 81% of the source by volume, with the remaining 19% of the source being KG2, which we refer to as pyroxenite.

3.1.2. Advantages and disadvantages of pMELTS for modelling

The pMELTS software was used to estimate the major and trace element composition of instantaneous fractional melts produced by adiabatic decompression of these two lithologies, specifically the most recent available version of the ALPHAMELTS front end available in June 2012 (Ghiorso et al., 2002; Smith and Asimow, 2005). While several parametrisations of peridotite melting are available, only a single mafic lithology, the G2 MORB composition, has been parametrised (Pertermann and Hirschmann, 2003). Use of pMELTS provides flexibility in terms of the provisional comparison of the melting behaviour of different lithologies. Furthermore, pMELTS tracks the residual mantle mineralogy during melting and calculates the trace element composition of instantaneous melts according to these shifts in mineralogy and the melting reaction. Such variations in mineralogy, such as the shift from garnet to spinel stability in the residue during decompression, or the disappearance of clinopyroxene from the residue, have important effects on the trace element contents of the instantaneous

fractional melts. These effects are crucial in controlling, for example, the differing behaviour of La and Yb which was noted in the melt inclusion observations. An advantage of pMELTS is that both the major and trace element composition of the instantaneous fractional melts can be predicted, meaning that the forsterite content of the first crystallising olivine for each primary melt packet can be calculated, allowing for comparison of model results with the observations of the covariation of trace element contents of melt inclusions with their host olivines. pMELTS also offers great flexibility in the specification of the pressure-temperature path followed by the mantle during melting. This flexibility allows us to consider the influence of the thermal effects of melting of the dominant peridotite lithology on the melting behaviour of the pyroxenite.

While the use of pMELTS provides flexibility in the melt modelling, there are some crucial aspects of the pMELTS results that must be treated with caution. These issues do not influence the general conclusions regarding the role of melt mixing, but certain aspects of the melting behaviour should not be regarded as robust features. The melts models are therefore largely used in an illustrative sense: development of accurate forward models of the melting of lithologically heterogeneous mantle is a long-term goal of igneous petrology that awaits improvement of the underlying thermodynamic models of the phases present during melting. The developers of pMELTS reported that for melting of peridotite lithologies the relationship between predicted melt fraction and temperature is offset from experimental results by up to 60°C such that melt fractions predicted from pMELTS at a given temperature are lower than those observed in laboratory experiments (Ghiorso et al., 2002). This problem clearly limits the usefulness of pMELTS when attempting to estimate mantle potential temperatures from natural basalt compositions. These features are also linked to an overestimation of the proportion of clinopyroxene in the solid residue and predicted liquid MgO contents that are significantly higher than the experimental products at small melt fraction, by as much as 3 wt% absolute. Nevertheless the patterns of major and trace element evolution as a function of extent of melting, the signs of slopes and kinks in the experimental data, are well reproduced by pMELTS. The near-solidus behaviour of pMELTS is also complicated by problems associated with nature of incorporation of minor elements such as Cr, K, and P into solid phases and has lead several authors to limit the use of these elements in their comparison of pMELTS predictions with experimental results (Lambart et al., 2012). Imperfections involved in the calculation of crystallisation paths of primitive basalt compositions by MELTS and pMELTS have been highlighted by Villiger et al. (2004). These authors demonstrated that pyroxenes are predicted as liquidus phases by MELTS and pMELTS under experimental conditions when olivine has been shown to be the liquidus phase. This overestimate of the proportion of pyroxene in the crystallising assemblage can drive the Si content of the predicted remaining liquid to values that are lower than those observed either in experimental studies or in natural basaltic suites.

Given these considerations, we do not use pMELTS for any crystallisation models, and do not use pMELTS models of mantle melting to constrain potential temperature or other bulk physical or chemical properties of the mantle. Instead, we use pMELTS in an illustrative fashion, to show how trace element and major element compositions of fractional melts might be expected to vary during decompression melting of a bi-lithological mantle. The major con-

clusions reached from the modelling presented below are robust to the limitations of pMELTS.

3.1.3. pMELTS modelling of melting of bi-lithological mantle

The melt modelling had to be carried out in a number of stages because pMELTS does not yet explicitly include an option for bi-lithological melting. Furthermore, the recommended maximum pressure of pMELTS calculations is 4 GPa, a constraint that limits the style of calculation of deep melting of fusible lithologies at elevated mantle potential temperature.

[Figure 6 about here.]

First, the melting calculations for isentropic decompression of the depleted mantle composition, DMM, were performed at a model potential temperature of 1512°C. This high potential temperature reflects the fact that the models results are eventually compared with observations from Iceland. The calculated solidus intersection pressure was 3.3 GPa (106 km depth) in this model but because a residual porosity of 0.5% was used, melt was only extracted from depths of 101 km and shallower (Figure 6). The maximum extent of melting was 30.3% at the top of the melting region at 1.0 GPa (25 km). The discontinuities in the gradient of the melt fraction against depth for DMM are related to the disappearance of solid phases from the residue: cpx-out at 78 km, garnet-out at 50 km and spinel-out at 38 km. The stability of garnet to such low pressures and the limited stability range of spinel partly reflects imperfections in the pMELTS garnet model, but also the fact that the DMM composition was limited to the system CFMAS-Mn, with the minor elements Na, K, P, Cr and Ni treated as trace elements (Smith and Asimow, 2005; Lambart et al., 2012). The disappearance of garnet from the solid assemblage leads to the peaks in the Y and Yb concentrations observed in the instantaneous fractional melts of DMM (Figure 6H,I). While it is likely that the depth of garnet-out and the peaks in heavy REEs and Y are deeper than 50 km under Iceland (Maclennan et al., 2003a), the crucial feature of the trace element distributions for the mixing models presented below is that the peak concentrations for the heavy REEs and Y occur shallower in the melting region, at higher extents of melting, than those for the light REEs. These REEs and other highly incompatible elements show their peak concentrations at the base of the melting region (Figure 6B-E).

The next stage of the melting calculations was to examine the isentropic decompression of the enriched KG2 composition. This material is more fusible than DMM and intersects its solidus at greater depth. Even after restricting the KG2 composition by removing Na and K from the suite of major elements, the solidus depth of KG2 is poorly defined and at much higher pressures than the recommended 4 GPa limit for pMELTS calculations. Fortunately, the solid phase assemblage for KG2 bulk composition is predicted to change very little over the pressure range from 3–5 GPa or more. The initial stage of melting of KG2 is therefore approximated by calculating the isobaric fractional melting behaviour at 3.3 GPa, the solidus pressure calculated for DMM on the adiabat corresponding to a potential temperature of 1512°C . The KG2 composition has melted by 19% at these solidus conditions for the DMM composition. The fractional melt compositions from this initial melting interval were then

stretched to depths between a KG2 solidus at 138 km and the DMM solidus at 106 km. The depth of the solidus of KG2 was set to occur at a pressure ~1 GPa greater than that of DMM and the solidus productivity was fixed at 13%/GPa, broadly following the findings of Pertermann and Hirschmann (2003). With knowledge of the solidus depth, the solidus productivity and the extent of melting at 106 km, it was possible to calculate a quadratic melt fraction against depth relationship for the initial melting interval and stretch the melt compositions from the isobaric calculations to their corresponding melt fraction.

The final melting calculation involved decompression melting of the solid residue of the isobaric melting of KG2. The decompression interval was from the solidus pressure of DMM to the lower pressure limit of pMELTS at 1 GPa. As described previously, it was assumed that the mass fraction of KG2 present in the melting mantle was small enough that the decompression path for both lithologies could be assumed to follow the melting isentrope of DMM. The melt fraction against depth curve for KG2 exhibits a number of steps in gradient not only as a result of the disappearance of solid phases from the KG2 residue but also in response to changes in gradient of the geotherm set from the DMM melting. The most important of these steps occurs at the solidus of DMM, where the productivity of KG2 drops significantly. This feature occurs because the onset of melting of the refractory DMM lithology draws latent heat from the mantle and causes an increase in the geothermal gradient. The predicted trace element behaviour of the KG2 melts shows a maximum for incompatibles at the base of the melting region and peaks in heavy REEs and Y at about 60 km depth after the disappearance of garnet from the solid residue (Figure 6). The key differences between the distribution of instantaneous fractional melt compositions for KG2 and DMM are first that the deeper onset of melting for KG2 means that the incompatible elements are transferred to the melt deeper and second that for most of the incompatible elements the concentrations from the first melts of KG2 are higher than those for DMM. The high concentrations of incompatible elements in the first melts of KG2 reflect the high concentrations in the KG2 source. These features, particularly the difference in the depth of transfer of the elements Pb, Sr and Nd for the KG2 and DMM lithologies, have important consequences for isotopic variation that is preserved during progressive melt mixing and for the interpretation of plots of isotopic data from individual volcanic systems or mid-ocean ridge segments. This crucial finding is explored in later sections.

3.1.4. Partition coefficients

The partition coefficients used in the trace element modelling are those dependent on pressure, temperature and composition, set as defaults in pMELTS (Smith and Asimow, 2005; Wood and Blundy, 1997). One trace element that is worth particular attention is Pb, not only because its isotopes are used to trace source variability but also because its partitioning behaviour during mantle melting is relatively poorly understood (Blundy and Wood, 2003). The relative constancy of Pb/Ce in oceanic basalts has been used to argue that the effective partition coefficient of Pb during mantle melting under ridges is similar to that of Ce (Hofmann, 1988). However, experimental partitioning studies have found that Pb is significantly more incompatible than Ce during peridotite melting (Salters, 2002). These authors suggested that the presence of trace sulphides in the peridotitic mantle may ac-

11

count for the mismatch between the observed uniformity of Ce/Pb and the experimentally determined partition coefficients. Alternatively, more recent experimental studies of Pb partitioning indicate that it may be more compatible than Ce during pyroxenite melting (Klemme et al., 2002; Elkins et al., 2008), raising the possibility that the apparent similarity in Ce and Pb behaviour reflects a balance of peridotite and pyroxenite in the mantle source regions. We therefore set the partition coefficients of Pb during DMM melting to be equal to the pMELTS predicted partition coefficient for Ce, and for melting of KG2 we used $D_{\mathrm{cpx}} = 0.04$, $D_{\mathrm{gt}} = 0.04$, $D_{\mathrm{opx}} = 0.01$ and $D_{\mathrm{ol}} = 0.005$.

The target of this modelling is to use the model fractional melt compositions as a template for understanding the covariation of elements and isotopes in samples from single volcanic systems, rather than matching average observed compositions or crustal thicknesses from Iceland. Nevertheless, the overall melt production for a triangular sub-ridge melting region containing 19% KG2 in a matrix of DMM provides a good, if non-unique, fit to the observed volume-averaged REE compositions from Theistareykir, such that the predicted concentrations are within 25% of those observed for all REEs (Maclennan et al., 2001a). In addition, the predicted crustal thickness is approximately 22 km, in good agreement with the observed crustal thickness under Theistareykir of $\sim$20 km (Staples et al., 1997).

3.1.5. Mean melt compositions

For each lithology j, the melting model provides two key functions: $X_j(z)$, the degree of melting at a depth z (as plotted in Figure 6), and $c_j(X)$, the concentration of the fractional melt produced at that depth. The pMELTS modelling described above provides $c_j(X)$ not only for a range of trace elements, but also for major elements including Mg and Fe, which are used to calculate the forsterite contents of olivines crystallising from the melts. The mean composition of the melt produced by lithology j is a weighted mean of the fractional melt compositions

$$\overline{C}_j = \frac{\displaystyle\int_0^{X_j^{\mathrm{max}}} \omega_j(X) c_j(X)\,\mathrm{d}X}{\displaystyle\int_0^{X_j^{\mathrm{max}}} \omega_j(X)\,\mathrm{d}X}, \tag{1}$$

where $\omega_j(X)$ is a weight function which differs depending on the style of melting considered: for a simple 1D melting column $\omega_j(X)$ is constant; for a triangular melting region $\omega_j(X)$ is the depth from the top of the melting region. X_j^{max} is the maximum degree of melting. (1) can be written is terms of normalised weights $\tilde{\omega}_j(X)$ as

$$\overline{C}_j = \int_0^{X_j^{\mathrm{max}}} \tilde{\omega}_j(X) c_j(X)\,\mathrm{d}X, \tag{2}$$

where

$$\tilde{\omega}_j(X) = \frac{\omega_j(X)}{\displaystyle\int_0^{X_j^{\mathrm{max}}} \omega_j(X)\,\mathrm{d}X}. \tag{3}$$

12

The mean composition of the total melt produced from all of the lithologies is a weighted mean of the $\overline{C}_j$,

$$\overline{\overline{C}} = \sum_{j=1}^{m} f_j \overline{C}_j, \tag{4}$$

where m is the number of lithologies ($m = 2$ for the calculations here). If the source contains proportions $\{p_1, \ldots, p_m\}$ of the different lithologies, the proportions f_j are given by

$$f_j = \frac{p_j \int_0^{X_j^{\max}} \omega_j(X) \, \mathrm{d}X}{\sum_{k=1}^{m} p_k \int_0^{X_k^{\max}} \omega_k(X) \, \mathrm{d}X}. \tag{5}$$

For computational convenience it is useful to divide the melting curve for each lithology into a discrete number of fractional melt "packets", where c_j^i is the concentration of the ith fractional melt packet produced by melting the jth lithology, $i = 1, \ldots, n_j$, $j = 1, \ldots, m$. n_j is the number of discrete melt packets produced from lithology j. ΔX_j is the degree of melting associated with each melt packet, and $X_j^i = (i - 1)\Delta X_j$ is the discretized degree of melting ($c_j^i = c_j(X_j^i)$). The total degree of melting of each lithology is $X_j^{\max} = n_j \Delta X_j$. ΔX_j is chosen to be small ($\Delta X_j = 0.01\%$) to provide an accurate approximation to the true fractional melt curve. In the limit that $\Delta X_j \to 0$ the continuous fractional melt distribution is recovered.

The discrete analogue of (2) is

$$\overline{C}_j = \sum_{i=1}^{n_j} \tilde{\omega}_j^i c_j^i \tag{6}$$

where the $\tilde{\omega}_j^i$ are normalised weights, $\omega_j^i = \omega_j(X_j^i)$,

$$\tilde{\omega}_j^i = \frac{\omega_j^i}{\sum_{i=1}^{n_j} \omega_j^i}. \tag{7}$$

The mean composition of the total melt is then

$$\overline{\overline{C}} = \sum_{j=1}^{m} \sum_{i=1}^{n_j} f_j \tilde{\omega}_j^i c_j^i, \tag{8}$$

i.e. a weighted average over the compositions of the individual fractional melt packets.

3.2. Mixing scheme

The mixing scheme proposed here considers each sample to be a particular mixture of fractional melts. The composition of a sample is thus a weighted average of the compositions of the individual fractional melt packets,

$$\hat{C} = \sum_{j=1}^{m} \sum_{i=1}^{n_j} \hat{r}_j^i c_j^i, \tag{9}$$

13

which is very similar to (8), except that the weights $\hat{r}^i_j$ are chosen randomly: the hats on $\hat{r}^i_j$ and $\hat{C}$ are used to signify that they are random variables. The probability distribution of the random weights $\hat{r}^i_j$ determines the amount and style of mixing. To be a valid mixture, the $\hat{r}^i_j$ must only take positive values and must satisfy the constant sum constraint,

$$\hat{r}^i_j \geq 0, \qquad \sum_{j=1}^{m}\sum_{i=1}^{n_j} \hat{r}^i_j = 1. \tag{10}$$

An additional constraint to place on the random weights $\hat{r}^i_j$ is that they should produce compositions that agree with (8) in the mean, i.e. $\mathbb{E}(\hat{C}) = \overline{\overline{C}}$, where $\mathbb{E}$ denotes expected value. This can be achieved by demanding that

$$\mathbb{E}(\hat{r}^i_j) = f_j \tilde{\omega}^i_j. \tag{11}$$

Within the restrictions placed by (10) and (11) there are a plethora of possible probability distributions for the weights $\hat{r}^i_j$. Amongst these possible distributions, there is one distribution that is particularly special. This distribution is the Dirichlet distribution, which has stronger independence properties amongst the weights $\hat{r}^i_j$ than all other possible distributions (see Appendix B for a summary of the properties of the Dirichlet distribution). These independence properties mean that all fractional melt packets are treated equally in the mixture, and in particular there is no depth-dependence to the mixing process. To satisfy (11), the weights $\hat{r}^i_j$ are formally distributed as a Dirichlet distribution with parameters α^i_j given by

$$\{\hat{r}^1_1, \ldots, \hat{r}^{n_1}_1, \ldots, \hat{r}^1_m, \ldots \hat{r}^{n_m}_m\} \sim \mathrm{Dir}\left(\alpha^1_1, \ldots, \alpha^{n_1}_1, \ldots, \alpha^1_m, \ldots, \alpha^{n_m}_m\right),$$
$$\alpha^i_j = (N-1)f_j\tilde{\omega}^i_j, \tag{12}$$

Using a Dirichlet distribution, once the mean composition is set by (11) there is only one further parameter controlling the distribution of the weights. This parameter is given in (12) as N, which we will term the mixing parameter, and varies from 1 to ∞. N controls the amount of mixing between the different fractional melts, with $N = 1$ representing no mixing and $N = \infty$ representing complete mixing. The behaviour of the Dirichlet distribution is illustrated in Figure 7 for a simpler case of three components (rather than the formally infinite number of components produced by fractional melting). Full details of the mixing scheme can be found in Appendix C.

[Figure 7 about here.]

The mixing parameter N is the key controlling parameter in the mixing scheme. When $N = 1$, the samples from the distribution are simply the individual fractional melt packets. When N is large, all samples have very similar compositions, close to that of the mean composition of the melt produced. The role of the mixing parameter N is perhaps best understood in terms of the effect it has on the variance of the sample concentrations,

$$\mathrm{var}(\hat{C}) \propto \frac{1}{N}, \tag{13}$$

14

i.e. large N implies small variance, well mixed. N is related to the mixing parameter M used by Maclennan (2008a) by $M = 1 - 1/N$ ($M = 0$ is unmixed, $M = 1$ is well-mixed).

The mixing parameter N used here is similar, but subtly different to, the mixing parameter N used in the work of Rudge et al. (2005) and Rudge (2006). In those papers, sampling is achieved by mixing together a discrete number N of independent identically distributed packets from a given distribution. The parameter N in Rudge et al. (2005) and Rudge (2006) is discrete, whereas the parameter N used in the Dirichlet mixing scheme proposed here is continuous (e.g. $N = 2.5$ is allowed). The mixing scheme of Rudge et al. (2005) and Rudge (2006) produces discrete distributions, as the proportions in which the different components are allowed to mix is discrete. The key advantage of the Dirichlet mixing scheme is that it produces continuous distributions. There are however strong similarities between the two mixing schemes: both have concentration variance $\propto 1/N$, and both approach normal distributions for large N. A more detailed discussion of the relationship between the two schemes can be found in Appendix F.

3.3. Homogenisation at depth

[Figure 8 about here.]

The Dirichlet distribution-based mixing scheme described above treats all fractional melt packets equally, independent of the depth at which they are generated. Thus as it stands the mixing scheme cannot be used to model depth-dependent mixing processes. To create a mixing scheme which includes some depth dependence in the mixing, in some model runs we include an additional process prior to applying the mixing scheme described above, namely a process of homogenisation at depth. We defer discussion of what physical mechanism may cause such a homogenisation to section 5. In the model runs with a homogenisation at depth the fractional melt distribution is altered before sampling so that all melts taken from below a certain prescribed depth are given a single composition equal to the appropriate weighted mean composition below that depth. An example of this process can be seen in Figure 8. The homogenisation at depth has the effect of removing a lot of the variability that is produced by the very first fractional melts that have the highest concentrations of incompatible elements. The fractional melts that are homogenised over have an equal contribution to every sample: an illustration of this can be seen in Figure 9, again for a simpler case of just three components.

[Figure 9 about here.]

3.4. Fractional crystallisation and concurrent mixing

In one of the model runs (Figure 13) a further process is included: fractional crystallisation and concurrent mixing. This is particularly important when considering the forsterite content of the olivines that host the melt inclusions, as fractional crystallisation then exerts a strong control. It is thought that samples that have undergone a greater degree of crystallisation are also likely to be more well mixed (Maclennan et al., 2003a). To model this, a standard uniform random variable is introduced

$$\hat{U} \sim \text{Uniform}(0, 1) \tag{14}$$

15

and functions are proposed that relate both the degree of crystallisation $\hat{\chi}$ and the mixing parameter $\hat{N}$ to this standard uniform random variable,

$$\hat{\chi} = \chi_{\max}\hat{U}^2, \tag{15}$$

$$\hat{N} = N_{\min}\left(\frac{N_{\max}}{N_{\min}}\right)^{\hat{U}}. \tag{16}$$

The functions above are somewhat ad hoc. They were chosen so that the degree of crystallisation varies from zero to some maximum value $\chi_{\max}$ (here $\chi_{\max} = 20\%$), and so that the mixing parameter varies from some minimum $N_{\min}$ to some maximum value $N_{\max}$. Of course, many other functions can be concocted that satisfy these properties: the above are chosen simply to demonstrate the main effects of concurrent mixing and crystallisation.

The compositions of the samples before crystallisation are generated just as before, except that $\hat{N}$ is now a random variable rather a parameter, and thus is different for each sample. The crystallisation is modelled using

$$\hat{C}_{\text{cryst-sample}} = \frac{\hat{C}}{1 - \hat{\chi}}, \tag{17}$$

$$\hat{\text{Fo}}_{\text{cryst-sample}} = \hat{\text{Fo}} - \alpha\hat{\chi}. \tag{18}$$

Equation (17) gives the concentration of the crystallised sample: for the purposes of this work it is assumed that La and Yb can be considered as perfectly incompatible when modelling crystallisation. Equation (18) states that the forsterite content of the crystallised sample decreases linearly with the degree of crystallisation. α is a parameter which governs this decrease (here $\alpha = 20$). The true dependence of forsterite content on degree of crystallisation is non-linear (see Maclennan et al. (2003a) for details), a linearisation is used here for simplicity.

4. Model results

4.1. Forsterite content – trace element systematics

[Figure 10 about here.]

[Figure 11 about here.]

Figures 10 and 11 show plots from model runs with La and Yb of variably mixed melts plotted against the forsterite content of olivines in equilibrium with these melts for different values of the mixing parameter N. Each point represents a random sample from the distribution, and each sub-plot shows 2000 such samples. The samples are colour-coded according to proportion by mass in which each lithology contributes to the sample, with dark blue being a pure melt from the peridotite and dark red a pure melt from the pyroxenite. When $N = 1$ each sample represents a single fractional melt, and lies on the curves expected for fractional melting (similar to Figure 5). For example, the first fractional melts of the peridotite will be highly concentrated in La (8 ppm) and be in equilibrium with $\sim$Fo$_{90}$ olivines. Later fractional melts will be much more depleted in La (tending to zero concentration) and be in

16

equilibrium with more forsteritic olivines. The first fractional melts of the pyroxenite will have even higher concentrations of La (20 ppm) (as the pyroxenite is rich in incompatible elements) but will be in equilibrium with less forsteritic olivines (at around Fo_{84}). Later fractional melts will be again more depleted in La, and again be in equilibrium with olivines with higher forsterite contents.

From each sub-plot to the next N doubles, each sub-plot representing more mixing having taken place than in the previous sub-plot. As the variance in concentration scales with $1/N$, each sub-plot has a reduction in standard deviation of $1/\sqrt{2}$ from the previous one. For large values of N the distributions appear elliptical on these plots as they approach the normal distribution behaviour expected from the central limit theorem. For large N, La shows a fairly strong negative correlation with forsterite content (correlation coefficient $r = -0.57$) whereas Yb is essentially uncorrelated ($r = 0.16$).

[Figure 12 about here.]

For comparison with the data shown in Figure 4, Figure 12 shows La and Yb of the mixed melts plotted against the forsterite content of the equilibrium olivine for a moderate value of the mixing parameter $N = 12$, alongside the standard deviation in La and Yb concentrations at fixed forsterite contents. Unlike the simple binary mixing models of Figure 23 there is now a distinct difference in behaviour between La and Yb, more in line with what is seen in the observations (Figure 4). As the forsterite content of the olivine decreases there is a distinct increase in the variance in La concentration of the equilibrium melts whereas the variance in Yb concentration of these melts decreases.

[Figure 13 about here.]

Figure 13 shows a model run that includes the effect of concurrent mixing and crystallisation, as discussed in section 2.2. The mixing parameter increases from $N = 12$ with no crystallisation to $N = 108$ at 20% crystallisation (a factor of 3 reduction in the concentration standard deviation). Figure 13 reproduces some of the key features seen in the observations of Figure 4: a peak in La variance around Fo_{89} and steady decline in Yb variance with decreasing forsterite content. Hence models of melting a compositionally heterogeneous source can account for the main features of the observations presented in Figure 4, although it should be noted that they equally may well be explained by melting a homogeneous source (Maclennan et al., 2003a).

4.2. Isotope – trace element systematics

[Figure 14 about here.]

The main motivation for studying the melting of a heterogeneous source is to examine the link between trace element and isotope systematics, which we turn to now. Figure 14 shows a plot of La/Nd against $^{143}Nd/^{144}Nd$ for model runs with different values of the mixing parameter N, to be compared with the data in Figure 2. The $N = 1$ case again shows the fractional melts. The peridotite source has a depleted isotopic signature ($^{143}Nd/^{144}Nd$=0.5133), the pyroxenite source an enriched signature ($^{143}Nd/^{144}Nd$=0.5129). Since the melting process does not fractionate ^{143}Nd from ^{144}Nd the fractional melts preserve the isotopic ratios of

17

their sources and thus appear as vertical lines in Figure 2. As in Figures 10 and 11, mixing reduces the variance and the distribution starts to resemble a bivariate normal distribution.

A key difference should be noted between the model and the data: In the data shown in Figure 2 there is a strong negative correlation between La/Nd and ^{143}Nd/^{144}Nd, whereas the model shown in Figure 14 predicts very little correlation ($r = 0.05$). This is a general feature: real data often show much better correlations than would be expected from a straightforward mixing of the fractional melts.

[Figure 15 about here.]

One way of producing better correlations is by altering the way mixing takes place. This is achieved in the model by homogenising at a depth of 85 km before Dirichlet sampling (see description in subsection 3.3). The effect of homogenisation at depth is illustrated in Figure 15 which shows a plot of the correlation coefficients amongst different trace element concentrations and isotopic ratios with and without a homogenisation at depth. Unsurprisingly, Figure 15 shows that trace elements with similar compatibilities correlate well with one another. The correlation pattern amongst the trace elements is independent of the mixing parameter N, but is substantially altered by the homogenisation at depth. This is particularly noticeable amongst the more incompatible elements (Hf to U), and arises because the situation essentially resembles that of binary mixing: Deep melts which are homogenised over have uniform concentrations of highly incompatible elements, shallow melts have effectively zero concentrations of highly incompatible elements. The samples are simply a binary mixture between one effective end member with uniform concentrations and another with concentrations close to zero.

[Figure 16 about here.]

Figure 16 shows a plot similar to Figure 14 which includes homogenisation at a depth of 85 km. The effect of the homogenisation can most clearly be seen in the $N = 1$ sub-plot in Figure 16. The most extreme La/Nd ratios have disappeared from those seen in Figure 14 since they represent the deepest fractional melts. In their place is a single point at ^{143}Nd/^{144}Nd=0.5130, La/Nd=0.4 (circled) representing the homogenisation of the deep fractional melts below 85 km. The shallower fractional melts remain unhomogenised, having lower La/Nd ratios and the isotopic ratios of the original sources. Importantly, for large N there is now a stronger inverse correlation between La/Nd and ^{143}Nd/^{144}Nd ($r = -0.87$), more like that seen in the real data (Figure 2). Encouragingly, the scatter away from a single binary mixing line which is observed in the data is also reproduced by this model. It is important to realise that such scatter away from the binary mixing trend is produced on these plots by a melt mixing model where only two source compositions are present. This model result indicates that observation of scatter on such trace element-isotope plots on MORB or OIB datasets need not require the presence of three or more source compositions in the associated mantle melting region.

This strong inverse correlation can be thought of as a consequence of creating a pseudo-binary mixing situation. In the $N = 1$ sub-plot of Figure 16 there are effectively three end-members: the homogenised deep melts (the circled green point), the shallow melts from the

18

pyroxenite (dark red points), and the shallow melts from the peridotite (dark blue points, which have some spread in La/Nd). The shallow melts from the pyroxenite are formed after the pyroxenite has undergone a degree of melting of 20% (Figure 6) and will have next to no La and very small amounts of Nd. The shallow melts of the peridotite are formed after the peridotite has undergone a degree of melting of only 5% and thus will have greater concentrations of both La and Nd than the shallow melts of pyroxenite. The highest concentrations of La and Nd are in the homogenised deep melts. Since the shallow pyroxenitic melts have such limited concentrations of La and Nd, and since the source is mostly peridotite (more than 80%), the mixing array is dominated by pseudo-binary mixing between the homogenised deep melts and the shallow melts from the peridotite. Note also that binary mixing lines are linear on this plot due to the common denominator Nd (Vollmer, 1976; Langmuir et al., 1978).

[Figure 17 about here.]

A homogenisation depth of 85 km is used throughout this work. We have experimented with this depth and found it to be a reasonable value for producing the desired pseudo-binary trends. The effect of varying the homogenisation depth can be seen in Figure 17. Setting the homogenisation depth below the onset of peridotite melting does not significantly change correlations from the unhomogenised case as a substantial proportion of the variance in trace element concentration is generated by fractional melting of the peridotite which is more than 80% of the source (top panels of Figure 17). If the homogenisation depth is set much shallower than 85 km then the shallow peridotite melts become too depleted in incompatible elements to have much influence, and the correlations seen in plots such as Figure 16 become worse (bottom panels of Figure 17). Given the limitations of the pMELTS modelling, as described in section 3.1.2, our preferred homogenisation depth of 85 km is not likely to have physical significance in melt generation and mixing under Iceland. A more robust conclusion is that the strength of correlations found in the observations are matched when all melts produced at depths greater than the point where the peridotite matrix has undergone ∼5% melting are mixed before extraction. As discussed in later sections, this feature of the model results is likely to have significance for understanding the physics of melt extraction under Iceland.

[Figure 18 about here.]

[Figure 19 about here.]

Figures 18 and 19 show plots similar to Figures 14 and 16 for La/Yb plotted against ^{143}Nd/^{144}Nd. There is a similar change in the correlation structure on homogenisation at depth: going from essentially zero correlation without homogenisation at depth to moderate negative correlation ($r = -0.31$) with. Interestingly, the model data show a triangular structure for intermediate values of N (Figure 19), with greater variance in La/Yb at low values of ^{143}Nd/^{144}Nd than at high values. This triangular structure is a feature also seen in the real data (Figure 2) although not a perfect match. The difference between the plots of La/Nd in Figure 16 and La/Yb in Figure 19 lies in the fact that Yb is much more compatible than Nd. As a result the shallow melts of the pyroxenite have significant concentrations of Yb

19

and the resulting mixing is more pseudo-ternary than pseudo-binary with the shallow melts of the pyroxenite having an influence. Mixtures with significant amounts of the pyroxenitic shallow melts will be pulled down to low values of La/Yb but their ^{143}Nd/^{144}Nd values will be largely set by the Nd-bearing homogenised deep melts and peridotitic shallow melts.

[Figure 20 about here.]

A further model run is shown in Figure 20 that plots Nb, Y, La/Yb and Sm/Yb against ^{208}Pb/^{206}Pb for $N = 5$ and a homogenisation depth of 85 km, to be compared with the real data in Figure 1. As can be seen in Figure 15, after homogenisation at depth, the lead isotopes show a reasonable correlation with Nb and other highly incompatible elements, but correlate less well with the more compatible elements such as Y. The Nb versus ^{208}Pb/^{206}Pb plot in Figure 20 bears some similarity with the data shown in Figure 1, although is not a perfect match. A notable similarity between model and data is that at low ^{208}Pb/^{206}Pb there is more variance in Nb concentrations than at high ^{208}Pb/^{206}Pb. The curved nature of the array is somewhat also similar to a hyperbolic binary mixing line, and may explain why a binary mixing model works so well for the real data (Figure 1). Like the real data, the plots of Y and Sm/Yb against ^{208}Pb/^{206}Pb are more diffuse.

The Nb against ^{208}Pb/^{206}Pb plot (Figure 20A) can be understood in terms of mixing between the three effective end members of the homogenised deep melts, the shallow melts from the pyroxenite, and the shallow melts from the peridotite. The homogenised deep melts have high Nb concentrations (4 ppm) and ^{208}Pb/^{206}Pb=2.02. The shallow melts from the peridotite have less Nb (< 1 ppm) and ^{208}Pb/^{206}Pb=2.28. Mixing between homogenised deep melts and the shallow peridotitic melts must lie on hyperbolic mixing lines between the two points with curvature controlled by the relative concentrations of Pb: The homogenised deep melts have Pb concentrations more than a factor of 10 greater than the shallow peridotitic melts, leading to a series of possible convex curves between the two points for mixtures to lie on. The situation is slightly complicated by the additional mixing in of the pyroxenitic shallow melts: unlike in the ratio plot of Figure 16 the pyroxenitic shallow melts play more of a role because a concentration is plotted on the vertical axis rather than a ratio. The pyroxenitic shallow melts have very little Pb so do not affect the Pb isotopes, but the fact they have next to no Nb causes them to reduce the Nb concentration at fixed ^{208}Pb/^{206}Pb on the plot, leading to the triangular shape of the array.

The Y against ^{208}Pb/^{206}Pb plot (Figure 20B) can not be thought of in terms of mixing between simple end members. Since Y is relatively compatible, both the shallow pyroxenitic and the shallow peridotitic melts exhibit a wide range in Y concentrations (from 0 to 80 ppm for the pyroxenitic melts, and from 0 to 100 ppm for the peridotitic melts, see Figure 6H) and thus cannot be thought of as simple end members. This is the reason for the more diffuse distribution in Y versus ^{208}Pb/^{206}Pb. The variance in Y is highest at low ^{208}Pb/^{206}Pb: this can be understood in terms of mixing between the homogenised deep melts (^{208}Pb/^{206}Pb=2.02, Yb=14 ppm) and the very shallow (< 75 km) melts from the peridotite and pyroxenite. These very shallow melts have a wide range of Y concentrations (from 0 to 100 ppm) but no Pb. They thus cause a large variability in Y concentration with no variability in ^{208}Pb/^{206}Pb. In order to produce compositions with larger ^{208}Pb/^{206}Pb some mixing in of the unhomogenised melts of the peridotite from around 85 to 75 km is required, which have almost uniform concentration of Y of around 11 ppm.

The apparent binary mixing observed in the data on the plots of La/Yb or Nb against ^{208}Pb/^{206}Pb can only be matched by the mixing models under a certain set of circumstances. First, the Pb concentrations in the deep homogenised melts must be 10 or more times higher than those in the shallow unhomogenised melts from the peridotite (this produces curvature on the pseudo-binary mixing line). Second, the Pb concentrations of the shallow unhomogenised melts from the pyroxenite should be very close to zero (so they do not affect the Pb isotopic compositions). Finally, the Nb and La concentrations of the shallow unhomogenised melts from both lithologies should be close to zero (to match the samples that have high Pb isotopic ratios but very low Nb and La/Yb). There are important trade-offs between the depth of homogenisation, the partition coefficients for the elements in the lithologies and the source concentrations of the elements in models that successfully reproduce the observations. Since the details of these trade-offs are dependent on variables that are not well constrained in the source regions, the primary purpose of the models is to illustrate that mixing of fractional melts from a bi-lithological mantle can account both for the apparent binary mixing in plots like Figure 1A and the scatter in Figure 1D. Nevertheless, one robust feature of successful mixing models is that the depth of homogenisation occurs after only a small fraction of melting of the depleted peridotite matrix: this feature is required to supply the Pb for the apparent depleted end-member on these plots.

4.3. Isotope systematics

[Figure 21 about here.]

[Figure 22 about here.]

Mixing of fractional melts complicates the interpretation of isotope ratio-isotope ratio plots, examples of which are shown in Figures 21 and 22. These plots again show the effect of mixing for different values of the mixing parameter N, with and without homogenisation at depth. The model runs demonstrate an important point that mixing arrays need not point towards the source compositions, even when only two end-member isotopic compositions are present in the mantle source. This phenomenon holds true even for melting a uniform lithology, and an analytical demonstration of this is given in Appendix E.

Without homogenisation at depth (Figure 21), there are just two points on the $N = 1$ subplot given by the isotopic ratios of the two sources (the crosses). The $N = 2$ subplot demonstrates the wide range of compositions that can be produced by mixing the fractional melts: in effect any of the points on any of the mixing hyperbolae between the two crosses is possible. This can be understood by considering the binary mixing hyperbola between a single fractional melt from the peridotite and a single fractional melt from the pyroxenite. The curvature of this mixing hyperbola is controlled by the ratio γ of Sr/Nd ratios of the two fractional melts, namely (Vollmer, 1976; Langmuir et al., 1978)

$$\gamma = \frac{(\text{Sr/Nd})_{\text{pyroxenite melt}}}{(\text{Sr/Nd})_{\text{peridotite melt}}}. \tag{19}$$

When $\gamma = 1$ the mixing hyperbola is a straight line; for $\gamma < 1$ it is convex (bending below a straight line between the two source compositions); and for $\gamma > 1$ it is concave (bending above). Examples of the binary mixing curves are shown in the $N = 1$ subplot of Figure 21.

21

As Sr is more incompatible than Nd, the Sr/Nd ratio is variable amongst the different fractional melts, varying for both peridotite and pyroxenite from around Sr/Nd=30 near the onset of melting to Sr/Nd=0 for the shallowest fractional melts (Figure 6E,F). As a result it is possible to get any value of γ by suitably choosing the depths of the two fractional melts. To get a large value of $\gamma \gg 1$ one can pick a deep melt from the pyroxenite (Sr/Nd around 30) and a shallow melt from the peridotite (Sr/Nd near zero). Likewise, to get a small value of $\gamma \ll 1$ one can pick a shallow melt from the pyroxenite (Sr/Nd near zero) and a deep melt from the peridotite (Sr/Nd around 30). By mixing the two chosen fractional melts in different proportions it is possible to be at any point along the given binary mixing hyperbola. Each point in the $N = 2$ subplot actually involves mixing between the whole distribution of possible fractional melts, rather than just two, but the simple mixing of two fractional melts demonstrates how such a large range of compositions is possible.

As N increases a bivariate normal distribution is recovered. The slope of the mixing array is somewhat shallower than that for a line through the two source compositions. In simpler single lithology models (details in Appendix E), this shift in the slope is purely controlled by the relative compatibilities of the two elements in question (here Nd and Sr), as is the correlation coefficient. The more similar the compatibilities of the two elements in question, the closer the slope of the line will be to that of the line through the sources, and the closer the correlation coefficient to unity.

With the homogenisation at depth (Figure 22), there is an additional green point on the $N = 1$ sub-plot representing the composition of the homogenised deep melts. As N increases a bivariate normal distribution is again recovered, except now the slope of the array is steeper than the line through the sources. It is thus clear that identifying the end points of mixing arrays with the compositions of mantle sources is fraught with difficulty: even in the simplest case of a binary source there is no guarantee that the source compositions lie on the line through the data array, and moreover the sources can lie on different sides of the line depending on how the fractional melts are mixed. Only in isotope ratio- isotope ratio plots where the isotope ratios are of the same element (e.g. $^{207}Pb/^{204}Pb$ against $^{206}Pb/^{204}Pb$) are the arrays guaranteed to point at the source compositions. In addition there is the well-known problem of variance reduction: we don't know how much mixing has taken place (i.e. what N is) and thus how far away the true mantle source compositions lie from the array.

5. Discussion

The preceding section has examined how some of the general features of the geochemical systematics of oceanic basalts can be explained in terms of melting and mixing. Evidence has been provided for some form of homogenisation at depth, which raises the question as to what physical mechanism could cause such a homogenisation. One possibility is that the early melts of the pyroxenite are unable to escape because the surrounding peridotite has not yet begun to melt, causing a permeability barrier. Only once the peridotite crosses its solidus and begins to melt can channels nucleate to provide rapid transport to the surface (Lundstrom et al., 2000; Spiegelman and Kelemen, 2003; Weatherley and Katz, 2012; Mallik and Dasgupta, 2012). The trapped early melts of the pyroxenite will have time to mix and homogenise before transport to the surface, as may also the very earliest melts of the peridotite before the channels form. This mixing geometry is consistent with the homogenisation depth used

throughout this manuscript, which lies just above the depth at which the peridotite crosses its solidus. The models of Weatherley and Katz (2012) indicate that the homogenised deep melts may then be transported in relative isolation towards the shallow part of the system. These deep melts then mix with the shallow melts in crustal magma chambers, and the mixing parameter N may reflect the mixing that takes place there. However, there are other reasons to expect the deeper melts to be more homogenised that the shallower melts, not least of which is the simple fact that the deeper melts have a longer transport path from their formation to the surface, and hence more time to mix with other melts en route.

The statistical models of mixing presented here are in their infancy, and there is plenty of scope for further development. One possible avenue for future research is to look at alternatives to the Dirichlet distribution for drawing the random weights. The Dirichlet distribution is rather special, and has strong independence properties that make it unsuitable for modelling depth-dependent mixing processes. This restriction was overcome in this manuscript by first altering the fractional melt population through a simple homogenisation at depth, followed by an application of the Dirichlet sampling scheme, the combination of which can be thought of as producing a single distribution for the random weights that is different from the Dirichlet distribution. However, a much more general approach would be to directly consider alternative distributions for the random weights, rather than have this two step process. With a more general distribution for the random weights one could model a less abrupt transition in behaviour with depth.

The focus of this work has been to obtain general insights into the role of melt mixing in producing geochemical distributions, rather than to produce exact fits to real data. To this end, the melt model has been kept constant throughout this work, with the same degree of melting on average for all model runs. The source compositions too have remained constant. If a particular suite of observations of short-lengthscale geochemical variation is to be investigated with this mixing model it is first necessary to match the mean of the observations by an appropriate choice of degree of melting and source composition before trying to match the local variability by adjusting the mixing process.

In this manuscript we have looked at datasets from Iceland that are highly restricted in space and time, such as whole-rock samples from single volcanic systems, or suites of olivine-hosted melt inclusions from single eruptions. This restriction justifies our assumption that the average degree of melting is constant. In our model, heterogeneity arises purely from the incomplete mixing of fractional melts. This contrasts with a number of studies (e.g. Phipps Morgan, 1999; Ito and Mahoney, 2005a,b; Ingle et al., 2010) that have used models with complete mixing but varying degrees and styles of melting to explain the heterogeneity seen over larger geographical areas and in global data sets. Undoubtedly, the variation in the melting process is important at larger length scales, and an obvious avenue for future research would be to develop a model that has both a variation in the melting process and an incomplete mixing of the fractional melts.

6. Conclusions

The relationships between isotopes of incompatible elements in suites of closely-spaced, temporally restricted basalt samples from mid-ocean ridges and ocean islands are often described in terms of binary mixing between depleted and enriched melts or solid sources.

Binary mixing has also been used to account for the relationships between these isotopic ratios and the elemental concentrations or concentration ratios. However, binary mixing cannot account for the relationships between moderately incompatible trace elements and the isotopes of incompatible elements. Furthermore, the presence of widespread U-series disequilibrium in young basalts, and the systematics of trace element variation in olivine-hosted melt inclusions, indicate that part of the local compositional variation in basaltic suites is due to the mantle melting process.

A model of mixing of fractional melts from a bi-lithological mantle is able to account both for the apparent binary mixing relationships in incompatible elements and for the weaker co-variations observed for more compatible trace elements. In these models, enriched, fusible heterogeneities are carried in a depleted, refractory peridotite mantle matrix. Unconstrained mixing of fractional melts of these two lithologies produces weak correlations between incompatible elements and their isotopes which do not resemble the strong correlations observed in suites of basaltic samples or olivine-hosted melt inclusions. The observed correlations are matched, however, when deep melts produced from both lithologies are effectively homogenised before they mix with the range of fractional melt compositions produced in the shallow parts of the melting region. The best fits to the data are obtained when fractional melts produced deeper than the level at which the peridotite matrix has undergone $\sim 5\%$ melting are homogenised. This pattern of mixing allows for some variance to be derived from the incompatible elements still remaining in the peridotite residue at 5% melting. The weak covariance of more compatible elements (Y, Yb) with the incompatible elements is also accounted for by this mixing because these elements are released shallower in the melt region than the fixed depth of homogenisation. The model can also account for the observed decoupling of the evolution of variance of La and Yb as a function of host forsterite content in olivine-hosted melt inclusions.

The examples in this manuscript have hopefully made clear the importance of mixing in the interpretation of the geochemical systematics of oceanic basalts. Mixing plays a role not only in the obvious sense of reducing the variability of geochemical observations, but also in subtly changing the correlations between different variables. While this certainly creates problems for interpretation, it may also mean that the observed correlations and geochemical distributions can shed light on the physics of melting and melt migration processes. Indeed this work suggests it may be possible to constrain the depth at which channelised flow begins from such geochemical distributions. Homogenisation at depth can lead to the pseudo-binary nature of a number of geochemical plots whose end-members are not representative of the true mantle sources.

Acknowledgements

Appendix A. The failure of binary mixing to explain La-Yb-Fo systematics

It is natural to ask whether the differing behaviour of La and Yb in Figure 4 can be accounted for by binary mixing of two melts combined with fractional crystallisation. The key differences in the observations that need to be reproduced by the modelling can be understood by examining Figure 4B,D and noting that the standard deviation of La increases with decreasing forsterite content up to a peak around Fo_{88} whereas the standard deviation of Yb has a peak around Fo_{90} and a subsequent decrease with decreasing forsterite content.

[Figure 23 about here.]

In order to test whether these differing evolutions of standard deviation could be matched with binary mixing and fractional crystallisation, we developed a simple model. Melt inclusions with La/Yb close to the extremes of the Borgarhraun dataset and in suitably forsteritic olivines were taken as end-member melts and then were mixed together in varying proportions in order to produce an array of mantle melts on a binary mixing array (Figure 23). The melt inclusion used as a depleted end-member was hosted in a $Fo_{91.4}$ olivine while the inclusion used as the enriched end-member was found trapped in a $Fo_{88.5}$ olivine. For this very simple mixing model, it was assumed that there was not sufficient variation in the Mg and Fe contents of the mantle melts for there to be substantial non-linearity in the relationship between the proportion of depleted and enriched melts in the mixture and the forsterite content of the olivine crystallising from the mixed melt. In other words, olivines growing from a 50:50 mixture of the two melts were predicted to contain 90.1 mol% forsterite. Formally, the initial melt compositions and forsterite contents were determined by binary mixing as

$$\hat{C} = \hat{\rho}C_e + (1 - \hat{\rho})C_d, \tag{A.1}$$

$$\hat{Fo} = \hat{\rho}Fo_e + (1 - \hat{\rho})Fo_d, \tag{A.2}$$

where $\hat{\rho} \sim \text{Uniform}(0, 1)$ is a uniform random variable determining the proportion of the enriched end-member in the mixture, and 'e' and 'd' refer to the enriched and depleted compositions respectively. The mixed model mantle melts were then allowed to undergo variable extents of fractional crystallisation, up to a maximum of 35%. The crystallisation was modelled using using equations (17) and (18), with the random variable $\hat{\chi} \sim \text{Uniform}(0, 0.35)$.

A set of 500 random samples generated by this scheme is shown in Figure 23. Comparison of the results of the binary mixing model (Figure 23) with the Borgarhraun observations (Figure 4) is informative. Unsurprisingly, the binary mixing model can reproduce the steep increase in the maximum La of melts with decreasing forsterite content of the olivine host between Fo_{92} and Fo_{85}. The variations in the running means in panels A and C of Figures 4 and 23 are broadly similar, with a change in the gradient of the running means of both La and Yb at about 88 mol% forsterite. However, the evolution of the standard deviations in panels B and D of Figures 4 and 23 show two important differences between the model and the results.

The first key difference is that the standard deviation of both La and Yb increases with decreasing olivine host forsterite content in the models, while the observations both show dropping variance at forsterite contents of less than about 88 mol%. This mismatch is to be expected, because the model does not include the effects of concurrent mixing and

25

crystallisation, which acts to destroy variance in the melt inclusion compositions with lowering forsterite contents.

The second important difference between the observed and modelled evolution of standard deviations relates to the important decoupling of La and Yb in the observations, but the correlated behaviour of La and Yb in the binary mixing models. In the observations, Yb shows a peak in variability at close to Fo_{90}, while La variation remains high between Fo_{90} and Fo_{88}. The evolution of the variation in melt inclusion compositions with forsterite content can be understood as a balance between the destruction of variance by mixing and the generation of variance by the addition of compositionally variable mantle melts. The observation that variation in La is maintained between Fo_{90} and Fo_{88} implies that mantle melts with high La and in equilibrium with olivines with forsterite contents of < 90 mol% are supplied to the system. However, these melts cannot have extreme values of Yb or else they would contribute to variance in Yb and maintain a high standard deviation for Yb between Fo_{90} and Fo_{88}, which is contrary to observations. In the case of binary mixing, the enriched melts added are in equilibrium with $Fo_{88.5}$ olivines and their introduction helps to rapidly build variation both in La, because these melts have the highest La contents, and in Yb, because they are low in Yb. This building variability with decreasing forsterite content is displayed on panels B and D of Figure 23 between about Fo_{91} and $Fo_{88.5}$ in the models for both La and Yb. Therefore the binary mixing model cannot match the observed decoupling in the evolution of La and Yb variance because in the binary mixing model the enriched end-member has an extreme composition for both La (maximum) and Yb (minimum) and adds variability to both elements.

While binary mixing models can produce good fits to observed covariations of incompatible element concentrations, ratios and isotope ratios, they cannot account for the systematics of moderately compatible elements nor the evolution of variance in melt inclusion trace element concentrations as a function of their host olivine composition.

Appendix B. The Dirichlet distribution

The Dirichlet distribution is a continuous probability distribution that produces random proportions. It is characterised by a set of n parameters $\{\alpha_1, \alpha_2, \ldots, \alpha_n\}$ and has the probability density function,

$$f(x_1, \ldots, x_{n-1}; \alpha_1, \ldots, \alpha_n) \propto \prod_{i=1}^{n} x_i^{\alpha_i - 1}, \tag{B.1}$$

for all $x_1, \ldots, x_{n-1} > 0$ satisfying $x_1 + \ldots + x_{n-1} < 1$. The remaining component is given by the expression $x_n = 1 - x_1 - \ldots - x_{n-1}$.

A vector of random variables with a Dirichlet distribution, $\{\hat{\phi}_1, \hat{\phi}_2, \ldots \hat{\phi}_n\} \sim \text{Dir}(\alpha_1, \alpha_2, \ldots \alpha_n)$,

has moments

$$\mathbb{E}(\hat{\phi}_i) = w_i, \tag{B.2}$$

$$\mathrm{var}(\hat{\phi}_i) = \frac{w_i - w_i^2}{\alpha_0 + 1}, \tag{B.3}$$

$$\mathrm{cov}(\hat{\phi}_i, \hat{\phi}_j) = \frac{-w_i w_j}{\alpha_0 + 1}, \qquad (i \neq j). \tag{B.4}$$

where

$$\alpha_0 = \alpha_1 + \alpha_2 + \ldots + \alpha_n, \tag{B.5}$$

$$w_i = \frac{\alpha_i}{\alpha_0}. \tag{B.6}$$

Thus the w_i set the mean of the distribution, while the α_0 parameter has a key control on the variance.

The Dirichlet distribution is characterised by its very strong independence properties. In particular it has the property of complete neutrality, whereby each of the elements $\hat{\phi}_i$ of the random vector $\{\hat{\phi}_1, \hat{\phi}_2, \ldots \hat{\phi}_n\}$ are independent of the relative proportions of all the other elements. The very strong independence properties of the Dirichlet distribution are both a strength and a weakness (see Aitchison (1985) for a detailed discussion). A key limitation is that any two components of the Dirichlet vector must covary negatively (B.4): it cannot be used to model a situation with positive covariance.

A special case of the Dirichlet distribution is the symmetric Dirichlet distribution in which all the w_i are identical ($w_i = 1/n$). Then, for $\alpha_0 = n$, the distribution is uniform with each possible composition having equal probability. For $\alpha_0 < n$ the distribution is concentrated at the extremes of the simplex; for $\alpha_0 > n$ the distribution is concentrated near the mean.

The infinite dimensional generalisation of the Dirichlet distribution is the Dirichlet process. Formally, the model used here is based on the Dirichlet process, but has been discretized by the splitting into discrete melt packets. The discretized form is used here throughout because it is more amenable to numerical computation.

Appendix B.1. Random Dirichlet means

The mixing scheme used in this work exploits weighted sums of concentrations where the weights are generated randomly from the Dirichlet distribution (random Dirichlet means). It is thus useful to know the general properties of sums with Dirichlet weights.

Let $\{\hat{\phi}_1, \hat{\phi}_2, \ldots \hat{\phi}_n\} \sim \mathrm{Dir}(\alpha_1, \alpha_2, \ldots \alpha_n)$, and $\{\hat{y}_1, \hat{y}_2, \ldots \hat{y}_n\}$ be a set of independent (but not necessarily identically distributed) random variables. Assume that the $\hat{y}_i$ are independent of the $\hat{\phi}_i$. We are interested in the behaviour of the sum

$$\hat{Y} = \sum_{i=1}^{n} \hat{\phi}_i \hat{y}_i. \tag{B.7}$$

Using the expressions for the moments of the Dirichlet distribution given in (B.2), (B.3), and

(B.4), it can be shown that the moments of $\hat{Y}$ are given by

$$\mathbb{E}(\hat{Y}) = \sum_{i=1}^{n} w_i \mathbb{E}(\hat{y}_i), \tag{B.8}$$

$$\mathrm{var}(\hat{Y}) = \frac{1}{\alpha_0 + 1} \left(\sum_{i=1}^{n} w_i \left(\mathbb{E}(\hat{y}_i) - \mathbb{E}(\hat{Y}) \right)^2 + \sum_{i=1}^{n} w_i (1 + \alpha_0 w_i) \, \mathrm{var}(\hat{y}_i) \right). \tag{B.9}$$

Given two such sums

$$\hat{Y}^{(1)} = \sum_{i=1}^{n} \hat{\phi}_i \hat{y}_i^{(1)}, \qquad \hat{Y}^{(2)} = \sum_{i=1}^{n} \hat{\phi}_i \hat{y}_i^{(2)}, \tag{B.10}$$

their covariance is given by

$$\mathrm{cov}\left(\hat{Y}^{(1)}, \hat{Y}^{(2)}\right) = \frac{1}{\alpha_0 + 1} \left(\sum_{i=1}^{n} w_i \left(\mathbb{E}\left(\hat{y}_i^{(1)}\right) - \mathbb{E}\left(\hat{Y}^{(1)}\right) \right) \left(\mathbb{E}\left(\hat{y}_i^{(2)}\right) - \mathbb{E}\left(\hat{Y}^{(2)}\right) \right) \right.$$
$$\left. + \sum_{i=1}^{n} w_i (1 + \alpha_0 w_i) \, \mathrm{cov}\left(\hat{y}_i^{(1)}, \hat{y}_i^{(2)}\right) \right). \tag{B.11}$$

Further detailed discussion of random Dirichlet means can be found in Hjort and Ongaro (2005), which includes expressions for higher moments and a proof of asymptotic normality for large α_0.

Appendix B.2. Ratios of random Dirichlet means

We are also interested in the behaviour of ratios of sums, e.g. when considering the distribution of an isotopic ratio. Such ratios behave in a non-linear fashion, and their general behaviour can be quite complicated (see discussion in Rudge et al. (2005)). However, in some circumstances the behaviour of the ratio of sums can be linearised, and asymptotic expressions for the moments can be derived (see Appendix B of Rudge (2006)). Let

$$\hat{Y} = \sum_{i=1}^{n} \hat{\phi}_i \hat{y}_i, \qquad \hat{Z} = \sum_{i=1}^{n} \hat{\phi}_i \hat{z}_i, \tag{B.12}$$

and consider the ratio of sums

$$\hat{R} = \frac{\hat{Y}}{\hat{Z}}. \tag{B.13}$$

When $\alpha_0 \gg n$, we can linearise the ratio expression as

$$\hat{R} \sim \frac{\mathbb{E}(\hat{Y})}{\mathbb{E}(\hat{Z})} + \sum_{i=1}^{n} \hat{\phi}_i \hat{y}_i^{\star} \tag{B.14}$$

where

$$\hat{y}_i^{\star} = \frac{1}{\mathbb{E}(\hat{Z})} \left(\hat{y}_i - \frac{\mathbb{E}(\hat{Y})}{\mathbb{E}(\hat{Z})} \hat{z}_i \right). \tag{B.15}$$

Using the fact that

$$\mathbb{E}\left(\sum_{i=1}^{n} \hat{\phi}_i \hat{y}_i^\star\right) = 0, \tag{B.16}$$

and the expressions in (B.8) and (B.9), we have the following asymptotic expressions for the moments of $\hat{R}$,

$$\mathbb{E}(\hat{R}) \sim \frac{\mathbb{E}(\hat{Y})}{\mathbb{E}(\hat{Z})}, \tag{B.17}$$

$$\mathrm{var}(\hat{R}) \sim \frac{1}{\alpha_0 + 1}\left(\sum_{i=1}^{n} w_i\left(\mathbb{E}(\hat{y}_i^\star)\right)^2 + \sum_{i=1}^{n} w_i(1 + \alpha_0 w_i)\,\mathrm{var}(\hat{y}_i^\star)\right). \tag{B.18}$$

Similarly, from (B.11), the asymptotic covariance between two such ratios of sums is

$$\mathrm{cov}\left(\hat{R}^{(1)}, \hat{R}^{(2)}\right) \sim \frac{1}{\alpha_0 + 1}\left(\sum_{i=1}^{n} w_i\mathbb{E}\left(\hat{y}_i^{\star(1)}\right)\mathbb{E}\left(\hat{y}_i^{\star(2)}\right) + \sum_{i=1}^{n} w_i(1 + \alpha_0 w_i)\,\mathrm{cov}\left(\hat{y}_i^{\star(1)}, \hat{y}_i^{\star(2)}\right)\right). \tag{B.19}$$

Appendix C. Moments of the sample concentrations

We can use the general expressions for the moments of random Dirichlet means given in the preceding section to derive expressions for the moments of the sample distribution in our model. Given the discrete set of fractional melts c_j^i, i.e. the ith fractional melt from the jth lithology, the composition of the samples is determined according to the following scheme:

$$\{\hat{q}_j^1, \ldots, \hat{q}_j^{n_j}\} \sim \mathrm{Dir}\left((N-1)f_j\tilde{\omega}_j^1, \ldots, (N-1)f_j\tilde{\omega}_j^{n_j}\right), \tag{C.1}$$

$$\hat{\mathcal{C}}_j = \sum_{i=1}^{n_j} \hat{q}_j^i c_j^i, \tag{C.2}$$

$$\{\hat{p}_1, \ldots, \hat{p}_m\} \sim \mathrm{Dir}\left((N-1)f_1, \ldots, (N-1)f_m\right), \tag{C.3}$$

$$\hat{C} = \sum_{j=1}^{m} \hat{p}_j \hat{\mathcal{C}}_j, \tag{C.4}$$

where N is the mixing parameter, f_j is the expected proportion of melt arising from each lithology (see (5)), and n_j is the number of discrete fractional melt packets produced from each lithology. $\hat{\mathcal{C}}_j$ represents the composition of the melt produced from each lithology, whereas $\hat{C}$ is the final composition of the sample pooling melts from all the lithologies.

The mixing scheme (C.1-C.4) can also be written more concisely using a single set of Dirichlet weights $\hat{r}_j^i = \hat{p}_j \hat{q}_j^i$ as

$$\{\hat{r}_1^1, \ldots, \hat{r}_1^{n_1}, \ldots, \hat{r}_m^1, \ldots \hat{r}_m^{n_m}\} \sim \mathrm{Dir}\left(\alpha_1^1, \ldots, \alpha_1^{n_1}, \ldots, \alpha_m^1, \ldots, \alpha_m^{n_m}\right),$$
$$\alpha_j^i = (N-1)f_j\tilde{\omega}_j^i, \tag{C.5}$$

$$\hat{C} = \sum_{j=1}^{m}\sum_{i=1}^{n_j} \hat{r}_j^i c_j^i. \tag{C.6}$$

29

The fractional melts for each lithology have moments in discretized form as

$$\overline{C}_j = \sum_{i=1}^{n_j} \tilde{\omega}_j^i c_j^i \approx \int_0^{X_j^{\max}} \tilde{\omega}_j(X) c_j(X) \ \mathrm{d}X, \tag{C.7}$$

$$\sigma_j^2 = \sum_{i=1}^{n_j} \tilde{\omega}_j^i \left(c_j^i - \overline{C}_j\right)^2 \approx \int_0^{X_j^{\max}} \tilde{\omega}_j(X) \left(c_j(X) - \overline{C}_j\right)^2 \ \mathrm{d}X. \tag{C.8}$$

The moments of the sample composition have simple expressions in terms of the above fractional melt moments. The moments of $\hat{\mathcal{C}}_j$, the melt produced by each lithology, are given by applying (B.8) and (B.9) to (C.2) to yield

$$\mathbb{E}(\hat{\mathcal{C}}_j) = \overline{C}_j, \tag{C.9}$$

$$\mathrm{var}(\hat{\mathcal{C}}_j) = \frac{\sigma_j^2}{(N-1)f_j + 1}. \tag{C.10}$$

Combining the above expressions with (B.8), (B.9), and (C.4), yields the expressions for the sample moments as

$$\mathbb{E}(\hat{C}) = \sum_{j=1}^m f_j \overline{C}_j = \overline{\overline{C}}, \tag{C.11}$$

$$\mathrm{var}(\hat{C}) = \frac{1}{N} \left(\sum_{j=1}^m f_j \left(\overline{C}_j - \overline{\overline{C}}\right)^2 + \sum_{j=1}^m f_j \sigma_j^2 \right). \tag{C.12}$$

(C.11) demonstrates that the mean of the sample distribution is simply the appropriate weighted mean of the melts produced by each lithology. (C.12) shows that mixing reduces the variance by a factor of $1/N$ from that of the original fractional melt population, and divides the variance into two sources: the first sum in (C.12) represents the variance due to differences in the mean composition of melt *between* the different lithologies; the second sum represents the variance due to differences in fractional melt composition *within* each lithology.

For two elements, the covariance of $\hat{C}^{(1)}$ and $\hat{C}^{(2)}$ is, using (B.11),

$$\mathrm{cov}(\hat{C}^{(1)}, \hat{C}^{(2)}) = \frac{1}{N} \left(\sum_{j=1}^m f_j \left(\overline{C}_j^{(1)} - \overline{\overline{C}}^{(1)}\right) \left(\overline{C}_j^{(2)} - \overline{\overline{C}}^{(2)}\right) + \sum_{j=1}^m f_j \sigma_j^{(1,2)} \right), \tag{C.13}$$

where

$$\sigma_j^{(1,2)} = \sum_{i=1}^{n_j} \tilde{\omega}_j^i \left(c_j^{i(1)} - \overline{C}_j^{(1)}\right) \left(c_j^{i(2)} - \overline{C}_j^{(2)}\right) \tag{C.14}$$

$$\approx \int_0^{X_j^{\max}} \tilde{\omega}_j(X) \left(c_j^{(1)}(X) - \overline{C}_j^{(1)}\right) \left(c_j^{(2)}(X) - \overline{C}_j^{(2)}\right) \ \mathrm{d}X, \tag{C.15}$$

represents the covariance of the fractional melts produced from lithology j. The expression in (C.13) can be used to determine the expected correlation between different elements using

$$\text{cor}(\hat{C}^{(1)}, \hat{C}^{(2)}) = \frac{\text{cov}(\hat{C}^{(1)}, \hat{C}^{(2)})}{\sqrt{\text{var}\left(\hat{C}^{(1)}\right)\text{var}\left(\hat{C}^{(2)}\right)}}. \tag{C.16}$$

Importantly, this correlation will be independent of the mixing parameter N. Such correlations have been discussed in detail for the melting of a single lithology source by Slater et al. (2001).

Appendix D. Moments for a simple melting model

It is useful to examine the behaviour of a simple melting model, for which analytical expressions for the moments in the preceding section can be obtained. Consider the distribution of fractional melts produced by modal fractional melting with a constant partition coefficient,

$$c_j(X_j) = \frac{C_j^0}{D}(1 - X_j)^{1/D-1}, \tag{D.1}$$

where C_j^0 is the source concentration, D is the constant partition coefficient, and X_j is the degree of melting. Assuming a constant weight function (1D melting column), (C.7), (C.8), and (C.15) become

$$\overline{C}_j = \frac{C_j^0}{X_j^{\max}}\left(1 - (1 - X_j^{\max})^{1/D}\right), \tag{D.2}$$

$$\sigma_j^2 = \frac{(C_j^0)^2}{X_j^{\max}}\left(\frac{1 - (1 - X_j^{\max})^{2/D-1}}{D(2-D)} - \frac{\left(1 - (1 - X_j^{\max})^{1/D}\right)^2}{X_j^{\max}}\right), \tag{D.3}$$

$$\sigma_j^{(1,2)} = \frac{C_j^{0(1)}C_j^{0(2)}}{X_j^{\max}}\left(\frac{1 - (1 - X_j^{\max})^{1/D^{(1)}+1/D^{(2)}-1}}{D^{(1)} + D^{(2)} - D^{(1)}D^{(2)}} - \frac{\left(1 - (1 - X_j^{\max})^{1/D^{(1)}}\right)\left(1 - (1 - X_j^{\max})^{1/D^{(2)}}\right)}{X_j^{\max}}\right). \tag{D.4}$$

These expressions for the moments are somewhat cumbersome. More insightful expressions are obtained when it is assumed that the element in question is highly incompatible, so that $D \ll 1$. Then (D.2), (D.3), and (D.4) become

$$\overline{C}_j \sim \frac{C_j^0}{X_j^{\max}}, \tag{D.5}$$

$$\sigma_j^2 \sim \frac{(C_j^0)^2}{2X_j^{\max}D}, \tag{D.6}$$

$$\sigma_j^{(1,2)} \sim \frac{C_j^{0(1)}C_j^{0(2)}}{X_j^{\max}\left(D^{(1)} + D^{(2)}\right)}. \tag{D.7}$$

The correlation coefficient between two elements is given by

$$r_j^{(1,2)} = \frac{\sigma_j^{(1,2)}}{\sqrt{\sigma_j^{2(1)}\sigma_j^{2(2)}}} \sim \frac{2\sqrt{D^{(1)}D^{(2)}}}{D^{(1)} + D^{(2)}} = \frac{2\sqrt{D^{(2)}/D^{(1)}}}{1 + D^{(2)}/D^{(1)}}, \tag{D.8}$$

and depends only on the ratio of the two partition coefficients, $D^{(2)}/D^{(1)}$. Two elements with the same partition coefficient correlate perfectly ($r_j^{(1,2)} = 1$); the correlation decreases as $D^{(2)}/D^{(1)}$ increases or decreases away from 1. The slope of the geometric regression line in a plot of the concentration of one element against another is given by

$$\beta_j^{(1,2)} = \sqrt{\frac{\sigma_j^{2(2)}}{\sigma_j^{2(1)}}} \sim \frac{C_j^{0(2)}}{C_j^{0(1)}}\sqrt{\frac{D^{(1)}}{D^{(2)}}}, \tag{D.9}$$

and is similarly controlled by the ratio of the two partition coefficients.

Appendix E. Isotope ratio-isotope ratio plots

The effect seen in Figure 21, where a regression line through model data in an isotope ratio-isotope ratio plot does not go through the isotopic compositions of the sources, is a general feature of mixing of fractional melts and is not dependent on the two lithology nature of the source. Here we provide a simple analytical derivation of this effect assuming a single lithology source.

Let $\hat{y}^i$ and $\hat{z}^i$ represent the discrete fractional melt isotopic compositions (e.g. y could be ^{143}Nd and z could be ^{144}Nd). We are interested in the behaviour of the ratio of sums

$$\hat{R} = \frac{\hat{Y}}{\hat{Z}} = \frac{\sum_{i=1}^{n} \hat{q}^i \hat{y}^i}{\sum_{i=1}^{n} \hat{q}^i \hat{z}^i}. \tag{E.1}$$

Recalling the results from Appendix B.2, the random variable $\hat{R}$ has an asymptotic mean of

$$\mathbb{E}(\hat{R}) \sim \frac{\overline{y}}{\overline{z}}, \tag{E.2}$$

where $\overline{y} = \mathbb{E}(\hat{Y})$ and $\overline{z} = \mathbb{E}(\hat{Z})$, and an asymptotic variance

$$\text{var}(\hat{R}) \sim \frac{1}{N}\mathbb{E}(\hat{y}^{\star 2}), \tag{E.3}$$

where

$$\hat{y}^{\star} = \frac{\hat{z}}{\overline{z}}\left(\frac{\hat{y}}{\hat{z}} - \frac{\overline{y}}{\overline{z}}\right). \tag{E.4}$$

Suppose we sample the fractional melts from a binary source, where each source has a distinct but uniform isotopic composition. Suppose we have a probability f of sampling a melt from source a and a probability $1 - f$ of sampling a melt from source b. Then the isotopic ratio $\hat{y}/\hat{z}$ of the fractional melts will have a distribution

$$\frac{\hat{y}}{\hat{z}} = \begin{cases} (y/z)_a, & \text{with probability } f, \\ (y/z)_b, & \text{with probability } 1 - f, \end{cases} \tag{E.5}$$

where $(y/z)_a$ and $(y/z)_b$ are the isotopic ratios of the two sources. Note that

$$\mathbb{E}\left(\frac{\hat{y}}{\hat{z}}\right) = f\left(\frac{y}{z}\right)_a + (1-f)\left(\frac{y}{z}\right)_b. \tag{E.6}$$

We will assume that the concentrations $\hat{z}$ are independent of the isotopic ratios $\hat{y}/\hat{z}$. This assumption will not be valid in general, particularly not for multiple lithology sources, where isotopic ratios can correlate with source concentrations, but for simplicity it is assumed here. With this independence assumption we have that

$$\frac{\overline{y}}{\overline{z}} = \frac{\mathbb{E}(\hat{y})}{\mathbb{E}(\hat{z})} = \mathbb{E}\left(\frac{\hat{y}}{\hat{z}}\right) \tag{E.7}$$

and hence (E.5) may be rewritten using (E.6) and (E.7) as

$$\frac{\hat{y}}{\hat{z}} - \frac{\overline{y}}{\overline{z}} = \begin{cases} (1-f)\Delta, & \text{with probability } f, \\ -f\Delta, & \text{with probability } 1-f, \end{cases} \tag{E.8}$$

where Δ represents the difference in isotopic ratios between the two sources,

$$\Delta = \left(\frac{y}{z}\right)_a - \left(\frac{y}{z}\right)_b. \tag{E.9}$$

From (E.3), (E.4), and (E.8) it follows that

$$\mathrm{var}(\hat{R}) \sim \frac{1}{N}\mathbb{E}(\hat{y}^{\star 2}) = \frac{1}{N}\mathbb{E}\left[\left(\frac{\hat{y}}{\hat{z}} - \frac{\overline{y}}{\overline{z}}\right)^2\right]\mathbb{E}\left[(\hat{z}/\overline{z})^2\right] = \frac{f(1-f)\Delta^2}{N}\mathbb{E}\left[(\hat{z}/\overline{z})^2\right]. \tag{E.10}$$

Consider a plot of an isotopic ratio $\hat{R}^{(2)}$ (e.g. ^{143}Nd/^{144}Nd) against another isotopic ratio $\hat{R}^{(1)}$ (e.g. ^{87}Sr/^{86}Sr). The asymptotic mean of the model data will lie on the line going through the isotopic compositions of the two sources. However, the slope of the geometric regression line through the model data is given by

$$\beta = \sqrt{\frac{\mathrm{var}(\hat{R}^{(2)})}{\mathrm{var}(\hat{R}^{(1)})}} \sim \frac{\Delta^{(2)}}{\Delta^{(1)}}\sqrt{\frac{\mathbb{E}\left[\left(\hat{z}^{(2)}/\overline{z}^{(2)}\right)^2\right]}{\mathbb{E}\left[\left(\hat{z}^{(1)}/\overline{z}^{(1)}\right)^2\right]}} \tag{E.11}$$

and thus will not necessarily be the same as that of the slope of line through the two sources, which has slope $\Delta^{(2)}/\Delta^{(1)}$. The difference between the two slopes depends on the factor

$$\xi = \sqrt{\frac{\mathbb{E}\left[\left(\hat{z}^{(2)}/\overline{z}^{(2)}\right)^2\right]}{\mathbb{E}\left[\left(\hat{z}^{(1)}/\overline{z}^{(1)}\right)^2\right]}}. \tag{E.12}$$

For the simple melting model of section Appendix D, we have from (D.5) and (D.6) that

$$\mathbb{E}((\hat{z}/\overline{z})^2) \sim \frac{X^{\mathrm{max}}}{2D}. \tag{E.13}$$

33

and hence the factor ξ is given by the simple expression

$$\xi \sim \sqrt{\frac{D^{(1)}}{D^{(2)}}}. \tag{E.14}$$

Thus the adjustment in slope is purely controlled by the ratio of the partition coefficients of the two elements in question. For example, if $^{87}\text{Sr}/^{86}\text{Sr}$ is on the x-axis and $^{143}\text{Nd}/^{144}\text{Nd}$ is on the y-axis, then, since $D_{\text{Sr}} < D_{\text{Nd}}$, $\xi < 1$ and we expect the slope of the regression line to be shallower than the line which goes through the source compositions. A shallower slope for the regression line is also what is observed in Figure 21, although it should be noted that Figure 21 is for a two lithology case where the independence assumption leading to (E.7) may not be appropriate.

A simple expression can also be obtained for the correlation coefficient $r^{(1,2)}$ in the isotope ratio-isotope ratio plot. The asymptotic expression is

$$r^{(1,2)} \sim \frac{\mathbb{E}(\hat{y}^{\star(1)}\hat{y}^{\star(2)})}{\sqrt{\mathbb{E}((\hat{y}^{\star(1)})^2)\mathbb{E}((\hat{y}^{\star(2)})^2)}} = \text{sgn}(\Delta^{(1)}\Delta^{(2)})\frac{\mathbb{E}(\hat{z}^{(1)}\hat{z}^{(2)})}{\sqrt{\mathbb{E}((\hat{z}^{(1)})^2)\mathbb{E}((\hat{z}^{(2)})^2)}}. \tag{E.15}$$

For $D^{(1)}, D^{(2)} \ll 1$ the correlation coefficient takes the simple form

$$r^{(1,2)} \sim \text{sgn}(\Delta^{(1)}\Delta^{(2)})\frac{2\sqrt{(D^{(1)}/D^{(2)})}}{(1 + (D^{(1)}/D^{(2)}))}. \tag{E.16}$$

Thus, up to a sign, the correlation in a isotope ratio - isotope ratio plot is expected to be the same as that for the corresponding trace element - trace element plot (e.g. Nd against Sr). When the partition coefficients for both elements are the same, the regression line slope is the same as the line through the sources, i.e. $\xi = 1$, and the data correlates perfectly, i.e. $r^{(1,2)} = 1$. As $D^{(1)}/D^{(2)}$ decreases, the slope becomes shallower and the correlation becomes worse. For example, if $D^{(1)}/D^{(2)} = 1/2$, the slope is reduced by a factor $\xi = 1/\sqrt{2} \approx 0.71$ and the correlation coefficient has modulus $|r^{(1,2)}| = 2\sqrt{2}/3 \approx 0.94$.

Appendix F. The mixing scheme of Rudge et al. (2005)

[Figure 24 about here.]

In Rudge et al. (2005) and Rudge (2006) an alternative method of modelling mixing was proposed based on drawing a discrete number N of samples from a given distribution and then averaging. This mixing scheme is illustrated in Figure 24 for an underlying distribution of three components, similar to the Dirichlet distribution illustration of Figure 7. In the Rudge et al. (2005) mixing scheme the random weights $\hat{\psi}_i$ are given by the relative frequencies of a multinomial distribution,

$$\{\hat{m}_1, \hat{m}_2, \ldots, \hat{m}_n\} \sim \text{Multinomial}\left(N, [w_1, w_2, \ldots, w_n]\right), \tag{F.1}$$

$$\hat{\psi}_i = \frac{\hat{m}_i}{N}. \tag{F.2}$$

N determines the number of discrete samples that are drawn to produce the mixture and the $[w_1, w_2, \ldots, w_n]$ determine the probabilities of sampling each of the n components in the underlying distribution ($\sum_{i=1}^{n} w_i = 1$, $w_i \geq 0$).

The continuous Dirichlet mixing scheme of this work and the discrete mixing scheme of Rudge et al. (2005) are closely related, as the continuous Dirichlet distribution is known to be an approximation of the discrete multinomial distribution (Johnson, 1960). Consider the first and second moments of the multinomial proportions:

$$\mathbb{E}(\hat{\psi}_i) = w_i, \tag{F.3}$$

$$\text{var}(\hat{\psi}_i) = \frac{w_i - w_i^2}{N}, \tag{F.4}$$

$$\text{cov}(\hat{\psi}_i, \hat{\psi}_j) = \frac{-w_i w_j}{N}, \qquad (i \neq j). \tag{F.5}$$

These moments are identical to those of the Dirichlet distribution (B.2-B.4) with $\alpha_0 = N-1$. Hence any of the results which are based purely on the first and second moments (the means and covariances) will be exactly the same for the two mixing schemes. This includes all the results from the previous appendices. Differences between the two schemes arise in the higher moments (such as the skewness and kurtosis), which are different between the Dirichlet and multinomial distributions.

References

Abouchami, W., Galer, S.J.G., Hofmann, A.W., 2000. High precision lead isotope systematics of lavas from the Hawaiian Scientific Drilling Project. Chemical Geology 169, 187–209. doi:10.1016/S0009-2541(00)00328-4.

Abouchami, W., Hofmann, A.W., Galer, S.J.G., Frey, F.A., Eisele, J., Feigenson, M., 2005. Lead isotopes reveal bilateral asymmetry and vertical continuity in the Hawaiian mantle plume. Nature 434, 851–856. doi:10.1038/nature03402.

Aitchison, J., 1985. A general class of distributions on the simplex. J. Roy. Stat Soc. B 47, 136–146.

Blichert-Toft, J., Albarède, F., 2009. Mixing of isotopic heterogeneities in the Mauna Kea plume conduit. Earth and Planetary Science Letters 282, 190–200. doi:10.1016/j.epsl.2009.03.015.

Blundy, J., Wood, B., 2003. Mineral-melt partitioning of uranium, thorium and their daughters. Reviews in Mineralogy and Geochemistry 52, 59–123. doi:10.2113/0520059.

Chauvel, C., Hémond, C., 2000. Melting of a complete section of recycled oceanic crust: Trace element and Pb isotopic evidence from Iceland. Geochemistry Geophysics Geosystems 1, 1. doi:10.1029/1999GC000002.

Condomines, M., Morand, P., Alle'gre, C.J., Sigvaldason, G., 1981. 230Th-238U disequilibria in historical lavas from Iceland. Earth and Planetary Science Letters 55, 393–406.

Cordier, C., Benoit, M., Hémond, C., Dyment, J., Le Gall, B., Briais, A., Kitazawa, M., 2010. Time scales of melt extraction revealed by distribution of lava composition across a ridge axis. Geochemistry Geophysics Geosystems 11. doi:10.1029/2010GC003074.

Douglass, J., Schilling, J.G., 2000. Systematics of three-component, pseudo-binary mixing lines in 2D isotope ratio space representations and implications for mantle plume–ridge interaction. Chemical Geology 163, 1–23. doi:10.1016/S0009-2541(99)00070-4.

Elkins, L., Gaetani, G., Sims, K., 2008. Partitioning of U and Th during garnet pyroxenite partial melting: Constraints on the source of alkaline ocean island basalts. Earth and Planetary Science Letters 265, 270–286. doi:10.1016/j.epsl.2007.10.034.

Gast, P.W., 1968. Trace element fractionation and the origin of tholeiitic and alkaline magma types. Geochimica et Cosmochimica Acta 32, 1057–1086. doi:/10.1016/0016-7037(68)90108-7.

Ghiorso, M.S., Hirschmann, M.M., Reiners, P.W., Kress, V.C., 2002. The pMELTS: a revision of MELTS for improved calculation of phase relations and major element partitioning related to partial melting of the mantle to 3 GPa. Geochemistry Geophysics Geosystems 3, 1030. doi:10.1029/2001GC000217.

Hamelin, B., Dupré, B., Allègre, C.J., 1986. Pb–Sr–Nd isotopic data of Indian Ocean ridges: new evidence of large-scale mapping of mantle heterogeneities. Earth and Planetary Science Letters 76, 288–298. doi:10.1016/0012-821X(86)90080-4.

Hanano, D., Weis, D., Scoates, J.S., Aciego, S., DePaolo, D.J., 2010. Horizontal and vertical zoning of heterogeneities in the Hawaiian mantle plume from the geochemistry of consecutive postshield volcano pairs: Kohala-Mahukona and Mauna Kea-Hualalai. Geochemistry Geophysics Geosystems 11, Q01004. doi:10.1029/2009GC002782.

Hémond, C., Arndt, N.T., Litchenstein, U., Hofmann, A.W., Oskarsson, N., Steinthorsson, S., 1993. The heterogeneous Iceland plume: Nd-Sr-O isotopes and trace element constraints. Journal of Geophysical Research 98, 15833–15850. doi:10.1029/93JB01093.

Hirschmann, M.M., Stolper, E.M., 1996. A possible role for garnet pyroxenite in the origin of the "garnet signature" in MORB. Contributions to Mineralogy and Petrology 124, 185–208. doi:10.1007/s004100050184.

Hjort, N.L., Ongaro, A., 2005. Exact inference for random Dirichlet means. Statistical Inference for Stochastic Processes 8, 227–254. doi:10.1007/s11203-005-6068-7.

Hofmann, A., Jochum, K., Seufert, M., White, W., 1986. Nb and Pb in oceanic basalts: new constraints on mantle evolution. Earth and Planetary Science Letters 79, 33–45. doi:10.1016/0012-821X(86)90038-5.

Hofmann, A.W., 1988. Chemical differentiation of the Earth: the relationship between mantle, continental crust, and oceanic crust. Earth and Planetary Science Letters 90, 297–314. doi:10.1016/0012-821X(88)90132-X.

Ingle, S., Ito, G., Mahoney, J.J., Chazey, W., Sinton, J., Rotella, M., Christie, D.M., 2010. Mechanisms of geochemical and geophysical variations along the western Galápagos Spreading Center. Geochemistry Geophysics Geosystems 11, Q04003. doi:10.1029/2009GC002694.

Ito, G., Mahoney, J., 2005a. Flow and melting of a heterogeneous mantle: 1. Method and importance to the geochemistry of ocean island and mid-ocean ridge basalts. Earth and Planetary Science Letters 230, 29–46. doi:10.1016/j.epsl.2004.10.035.

Ito, G., Mahoney, J.J., 2005b. Flow and melting of a heterogeneous mantle: 2. Implications for a chemically nonlayered mantle. Earth and Planetary Science Letters 230, 47–63. doi:10.1016/j.epsl.2004.10.034.

Johnson, K.T.M., Dick, H.J.B., Shimizu, N., 1990. Melting in the oceanic upper mantle: An ion microprobe study of diopsides in abyssal peridotites. Journal of Geophysical Research 95, 2661–2678. doi:10.1029/JB095iB03p02661.

Johnson, N.L., 1960. An approximation to the multinomial distribution: Some properties and applications. Biometrika 47, 93–102.

Katz, R.F., Rudge, J.F., 2011. The energetics of melting fertile heterogeneities within the depleted mantle. Geochemistry Geophysics Geosystems 12, 1–22. doi:10.1029/2011GC003834.

Kelemen, P.B., Koga, K., Shimizu, N., 1997. Geochemistry of gabbro sills in the crust-mantle transition zone of the Oman ophiolite: Implications for the origin of the oceanic lower crust. Earth and Planetary Science Letters 146, 475–488. doi:10.1016/S0012-821X(96)00235-X.

Klemme, S., Blundy, J.D., Wood, B.J., 2002. Experimental constraints on major and trace element partitioning during partial melting of eclogite. Geochimica et Cosmochimica Acta 66, 3109–3123. doi:10.1016/S0016-7037(02)00859-1.

Kogiso, T., Hirose, K., Takahashi, E., 1998. Melting experiments on homogeneous mixtures of peridotite and basalt: application to the genesis of ocean island basalts. Earth and Planetary Science Letters 162, 45–61. doi:10.1016/S0012-821X(98)00156-3.

Kogiso, T., Hirschmann, M.M., Pertermann, M., 2004. High-pressure partial melting of mafic lithologies in the mantle. Journal of Petrology 45, 2407–2422. doi:10.1093/petrology/egh057.

Kokfelt, T.F., Hoernle, K., Hauff, F., Fiebig, J., Werner, R., Garbe-Schönberg, D., 2006. Combined trace element and Pb-Nd–Sr-O isotope evidence for recycled oceanic crust (upper and lower) in the Iceland mantle plume. Journal of Petrology 47, 1705–1749. doi:10.1093/petrology/egl025.

Koornneef, J., Stracke, A., Bourdon, B., Grönvold, K., 2012a. The influence of source heterogeneity on the U–Th–Pa–Ra disequilibria in post-glacial tholeiites from Iceland. Geochimica et Cosmochimica Acta 87, 243–266. doi:10.1016/j.gca.2012.03.041.

Koornneef, J.M., Stracke, A., Bourdon, B., Meier, M.A., Jochum, K.P., Stoll, B., Gronvold, K., 2012b. Melting of a two-component source beneath Iceland. Journal of Petrology 53, 127–157. doi:10.1093/petrology/egr059.

Lambart, S., Laporte, D., Provost, A., Schiano, P., 2012. Fate of pyroxenite-derived melts in the peridotitic mantle: thermodynamic and experimental constraints. Journal of Petrology 53, 451–476. doi:10.1093/petrology/egr068.

Langmuir, C.H., Vocke, R.D., Hanson, G.N., Hart, S.R., 1978. A general mixing equation with applications to Icelandic basalts. Earth and Planetary Science Letters 37, 380–392. doi:10.1016/0012-821X(78)90053-5.

Lundstrom, C., Gill, J., Williams, Q., 2000. A geochemically consistent hypothesis for MORB generation. Chemical Geology 162, 105–126. doi:10.1016/S0009-2541(99)00122-9.

Maclennan, J., 2008a. Concurrent mixing and cooling of melts under Iceland. Journal of Petrology 49, 1931–1953. doi:10.1093/petrology/egn052.

Maclennan, J., 2008b. Lead isotope variability in olivine-hosted melt inclusions from Iceland. Geochimica et Cosmochimica Acta 72, 4159–4176. doi:10.1016/j.gca.2008.05.034.

Maclennan, J., McKenzie, D., Gronvöld, K., 2001a. Plume-driven upwelling under central Iceland. Earth and Planetary Science Letters 194, 67–82. doi:10.1016/S0012-821X(01)00553-2.

Maclennan, J., McKenzie, D., Grönvold, K., Shimizu, N., Eiler, J.M., Kitchen, N., 2003a. Melt mixing and crystallization under Theistareykir, northeast Iceland. Geochemistry Geophysics Geosystems 4, 8624. doi:10.1029/2003GC000558.

Maclennan, J., McKenzie, D., Gronvöld, K., Slater, L., 2001b. Crustal accretion under Northern Iceland. Earth and Planetary Science Letters 191, 295–310. doi:10.1016/S0012-821X(01)00420-4.

Maclennan, J., McKenzie, D., Hilton, F., Gronvold, K., Shimizu, N., 2003b. Geochemical variability in a single flow from northern Iceland. Journal of Geophysical Research 108. doi:10.1029/2000JB000142.

Mallik, A., Dasgupta, R., 2012. Reaction between MORB-eclogite derived melts and fertile peridotite and generation of ocean island basalts. Earth and Planetary Science Letters 329-330, 97–108. doi:10.1016/j.epsl.2012.02.007.

McKenzie, D., 1985. The extraction of magma from the crust and mantle. Earth and Planetary Science Letters 74, 81–91. doi:10.1016/0012-821X(85)90168-2.

McKenzie, D., Stracke, A., Blichert-Toft, J., Albarède, F., Grönvold, K., O'Nions, R.K., 2004. Source enrichment processes responsible for isotopic anomalies in oceanic island basalts. Geochimica et Cosmochimica Acta 68, 2699–2724. doi:10.1016/j.gca.2003.10.029.

Peate, D.W., Baker, J.A., Jakobsson, S.P., Waight, T.E., Kent, A.J.R., Grassineau, N.V., Skovgaard, A.C., 2009. Historic magmatism on the Reykjanes Peninsula, Iceland: a snapshot of melt generation at a ridge segment. Contributions to Mineralogy and Petrology 157, 359–382. doi:10.1007/s00410-008-0339-4.

Pertermann, M., Hirschmann, M.M., 2003. Partial melting experiments on a MORB-like pyroxenite between 2 and 3 GPa: Constraints on the presence of pyroxenite in the basalt source regions from solidus location and melting rate. Journal of Geophysical Research 108. doi:10.1029/2000JB000118.

Phipps Morgan, J., 1999. Isotope topology of individual hotspot basalt arrays: Mixing curves or melt extraction trajectories? Geochemistry Geophysics Geosystems 1, 1003. doi:10.1029/1999GC000004.

Phipps Morgan, J., 2001. Thermodynamics of pressure release melting of a veined plum pudding mantle. Geochemistry Geophysics Geosystems 2. doi:10.1029/2000GC000049.

Rudge, J.F., 2006. Mantle pseudo-isochrons revisited. Earth and Planetary Science Letters 249, 494–513. doi:10.1016/j.epsl.2006.06.046.

Rudge, J.F., McKenzie, D., Haynes, P.H., 2005. A theoretical approach to understanding the isotopic heterogeneity of mid-ocean ridge basalt. Geochimica et Cosmochimica Acta 69, 3873–3887. doi:10.1016/j.gca.2005.03.004.

Sæmundsson, K., 1991. Jarðfræði kröflukerfisins. Náttúra Mývatns , 24–95.

Salters, V.J.M., 2002. Near mantle solidus trace element partitioning at pressures up to 3.4 GPa. Geochemistry Geophysics Geosystems 3, 1038. doi:10.1029/2001GC000148.

Salters, V.J.M., Stracke, A., 2004. Composition of the depleted mantle. Geochemistry Geophysics Geosystems 5, Q05B07. doi:10.1029/2003GC000597.

Shaw, D.M., 1970. Trace element fractionation during anatexis. Geochimica et Cosmochimica Acta 34, 237–243. doi:10.1016/0016-7037(70)90009-8.

Shorttle, O., Maclennan, J., 2011. Compositional trends of Icelandic basalts: Implications for short–length scale lithological heterogeneity in mantle plumes. Geochemistry Geophysics Geosystems 12, Q11008. doi:10.1029/2011GC003748.

Slater, L., McKenzie, D., Gronvöld, K., Shimizu, N., 2001. Melt generation and movement beneath Theistareykir, NE Iceland. Journal of Petrology 42, 321–354. doi:10.1093/petrology/42.2.321.

Sleep, N.H., 1984. Tapping of magmas from ubiquitous mantle heterogeneities: An alternative to mantle plumes? Journal of Geophysical Research 89, 10029. doi:10.1029/JB089iB12p10029.

Smith, P.M., Asimow, P.D., 2005. Adiabat_1ph: A new public front-end to the MELTS, pMELTS, and pHMELTS models. Geochemistry Geophysics Geosystems 6, Q02004. doi:10.1029/2004GC000816.

Sobolev, A.V., Shimizu, N., 1993. Ultra-depleted primary melt included in an olivine from the Mid-Atlantic Ridge. Nature 363, 151–154. doi:10.1038/363151a0.

Spiegelman, M., Kelemen, P.B., 2003. Extreme chemical variability as a consequence of channelized melt transport. Geochemistry Geophysics Geosystems 4, 1055. doi:10.1029/2002GC000336.

Staples, R.K., White, R.S., Brandsdóttir, B., Menke, W., Maguire, P.K.H., McBride, J.H., 1997. Färoe-Iceland Ridge Experiment 1. Crustal structure of northeastern Iceland. Journal of Geophysical Research 102, 7849–7866. doi:10.1029/96JB03911.

Stracke, A., Bizimis, M., Salters, V.J.M., 2003a. Recycling oceanic crust: Quantitative constraints. Geochemistry Geophysics Geosystems 4. doi:200310.1029/2001GC000223.

Stracke, A., Bourdon, B., 2009. The importance of melt extraction for tracing mantle heterogeneity. Geochimica et Cosmochimica Acta 73, 218–238. doi:10.1016/j.gca.2008.10.015.

Stracke, A., Salters, V.J.M., Sims, K.W.W., 1999. Assessing the presence of garnet-pyroxenite in the mantle sources of basalts through combined hafnium-neodymium-thorium isotope systematics. Geochemistry Geophysics Geosystems 1, 1. doi:10.1029/1999GC000013.

Stracke, A., Zindler, A., Salters, V., McKenzie, D., Blichert-Toft, J., Albarède, F., Grönvold, K., 2003b. Theistareykir revisited. Geochemistry Geophysics Geosystems 4, 8507. doi:10.1029/2001GC000201.

Stracke, A., Zindler, A., Salters, V.J.M., McKenzie, D., Grönvold, K., 2003c. The dynamics of melting beneath Theistareykir, northern Iceland. Geochemistry Geophysics Geosystems 4, 8513. doi:10.1029/2002GC000347.

Streckeisen, A., 1976. Classification of the Common Igneous Rocks by Means of Their Chemical Composition: A Provisional Attempt. Neues Jahrbuch fur Mineralogie, Monatshefte ; Heft 1.

Tanaka, R., Makishima, A., Nakamura, E., 2008. Hawaiian double volcanic chain triggered by an episodic involvement of recycled material: Constraints from temporal Sr-Nd-Hf-Pb isotopic trend of the Loa-type volcanoes. Earth and Planetary Science Letters 265, 450–465. doi:10.1016/j.epsl.2007.10.035.

Thirlwall, M.F., Gee, M.A.M., Taylor, R.N., Murton, B.J., 2004. Mantle components in Iceland and adjacent ridges investigated using double-spike Pb isotope ratios. Geochimica et Cosmochimica Acta 68, 361–386. doi:10.1016/S0016-7037(03)00424-1.

Villiger, S., Ulmer, P., Müntener, O., Thompson, A.B., 2004. The Liquid Line of Descent of Anhydrous, Mantle-Derived, Tholeiitic Liquids by Fractional and Equilibrium Crystallization–an Experimental Study at 1.0 GPa. Journal of Petrology 45, 2369–2388. doi:10.1093/petrology/egh042.

Vollmer, R., 1976. Rb-Sr and U-Th-Pb systematics of alkaline rocks: the alkaline rocks from Italy. Geochimica et Cosmochimica Acta 40, 283–295. doi:10.1016/0016-7037(76)90205-2.

Waters, C.L., Sims, K.W.W., Perfit, M.R., Blichert-Toft, J., Blusztajn, J., 2011. Perspective on the Genesis of E-MORB from Chemical and Isotopic Heterogeneity at 9-10 N East Pacific Rise. Journal of Petrology 52, 565–602. doi:10.1093/petrology/egq091.

Weatherley, S.M., Katz, R.F., 2012. Melting and channelized magmatic flow in chemically heterogeneous, upwelling mantle. Geochemistry Geophysics Geosystems doi:10.1029/2011GC003989.

Wood, B.J., Blundy, J.D., 1997. A predictive model for rare earth element partitioning between clinopyroxene and anhydrous silicate melt. Contributions to Mineralogy and Petrology 129, 166–181. doi:10.1007/s004100050330.

Workman, R.K., Hart, S.R., 2005. Major and trace element composition of the depleted MORB mantle (DMM). Earth and Planetary Science Letters 231, 53–72. doi:10.1016/j.epsl.2004.12.005.

1309 Zindler, A., Staudigel, H., Batiza, R., 1984. Isotope and trace element geochemistry of young
1310   Pacific seamounts: implications for the scale of upper mantle heterogeneity. Earth and
1311   Planetary Science Letters 70, 175–195. doi:10.1016/0012-821X(84)90004-9.
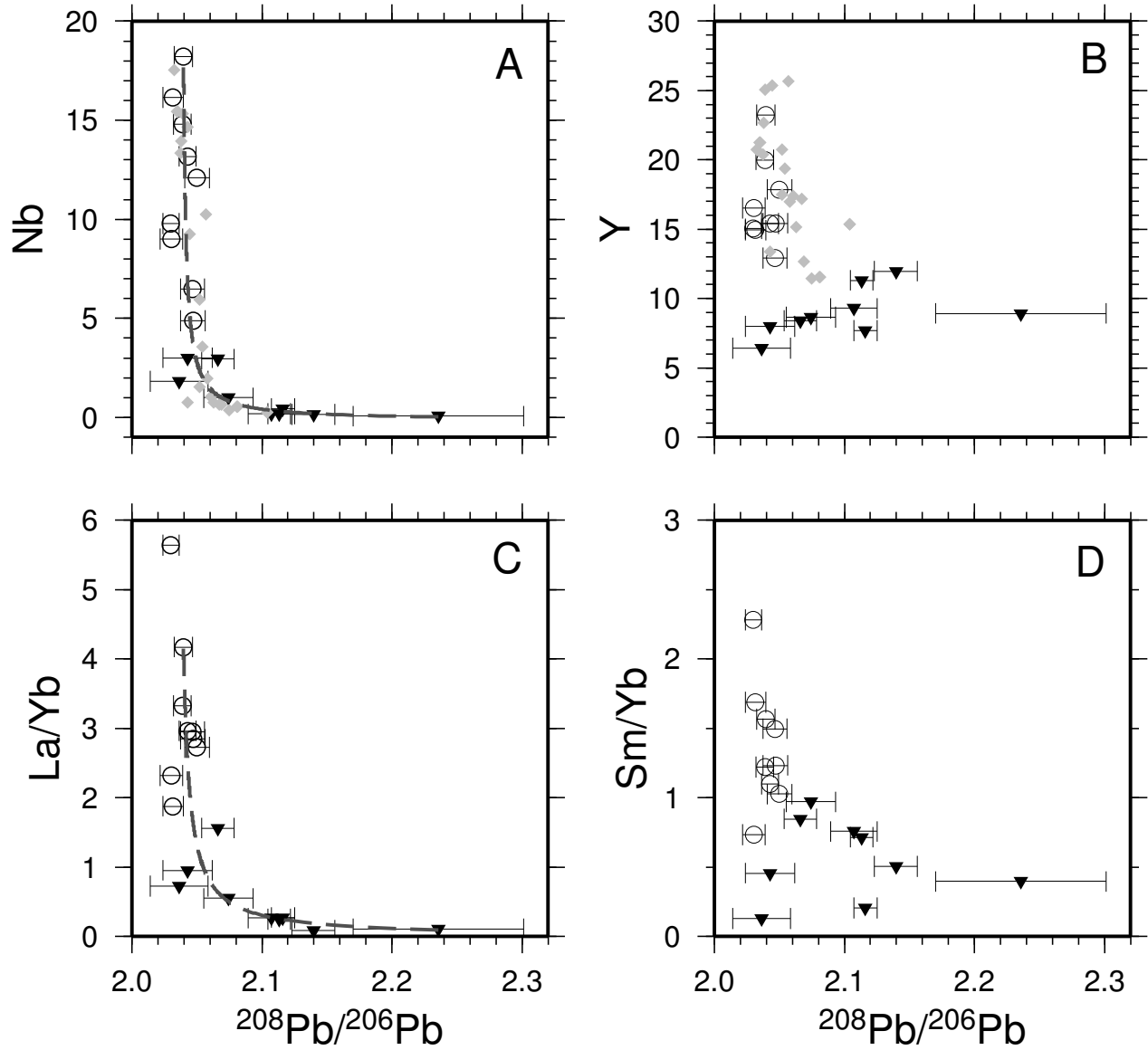
List of Figures

43

Figure 1: Relationships between trace element and isotopic compositions for Icelandic whole-rock samples and melt inclusions. Whole-rock data from the Reykjanes peninsula is shown as small grey diamonds. Olivine-hosted melt inclusion data from the Reykjanes Peninsula is shown as downwards pointing filled triangles for the Háleyjabunga eruption and unfilled circles for the Stapafell eruption. A binary mixing curve which provides a successful fit to the Reykjanes Peninsula data is shown as a grey dashed line on panels A and C. These curves are similar to those calculated by Maclennan (2008a), using extreme melt inclusion compositions as the mixing end-members and an assumption that the Pb concentration in the enriched end-member was 100 times higher than that in the depleted end-member. Data Sources: Kokfelt et al. (2006); Thirlwall et al. (2004); Maclennan (2008b)
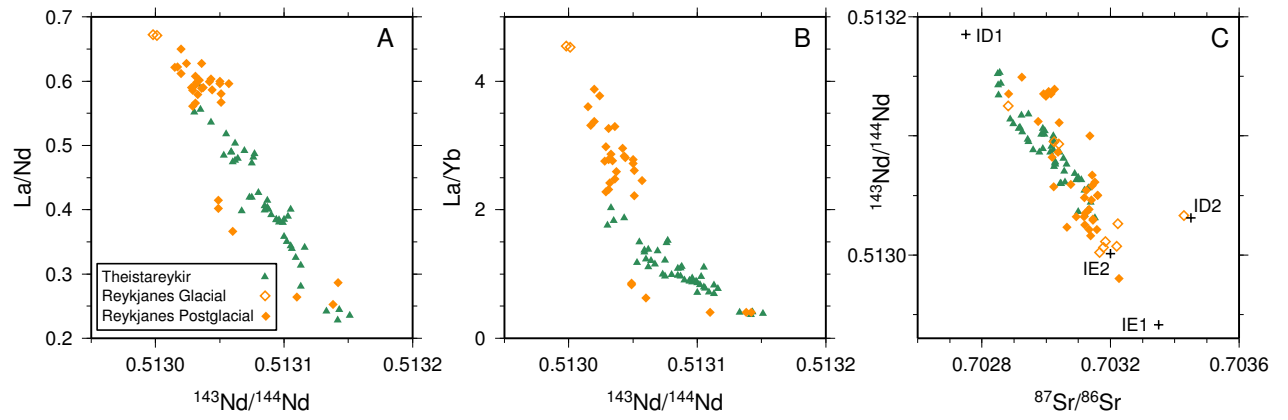
Figure 2: Trace element and isotope data for two Icelandic sample suites, from the Theistareykir volcanic system of northern Iceland, shown as green triangles, and the Reykjanes Peninsula of southwest Iceland, shown as orange diamonds. Samples of postglacial eruptions (i.e. > 12 kyr old) are shown with filled symbols and subglacial eruptions as outlines. Data for A and B from Koornneef et al. (2012b); Peate et al. (2009); Kokfelt et al. (2006); Stracke et al. (2003b); Chauvel and Hémond (2000); Hémond et al. (1993), with additional data from C from Thirlwall et al. (2004). The black crosses show four hypothetical mantle components proposed for Iceland by Thirlwall et al. (2004), two depleted components, ID1 and ID2 and two enriched components, IE1 and IE2.

49
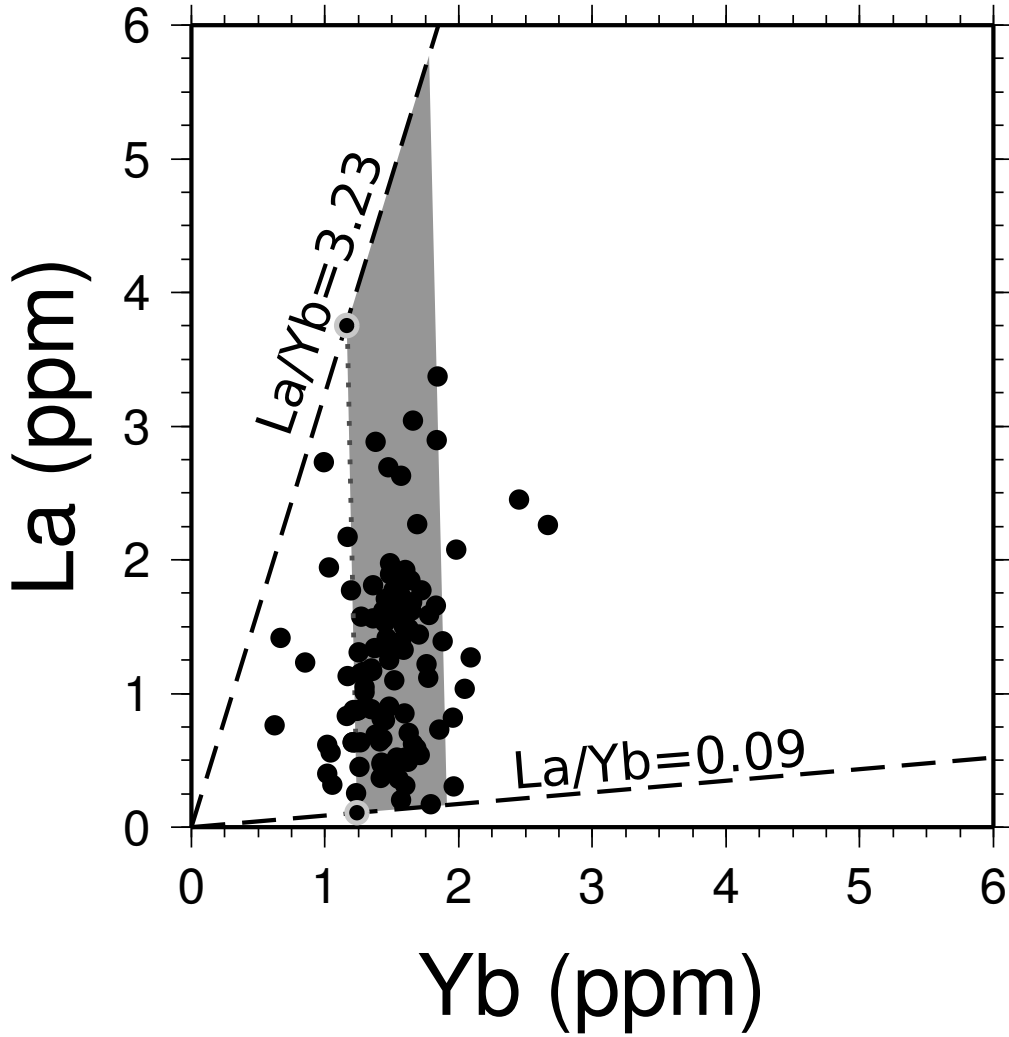
Figure 3: Trace element composition of olivine-hosted melt inclusions from the Borgarhraun flow in northern Iceland (Maclennan et al., 2003a) are shown as black circles. These inclusions are hosted in olivines whose forsterite content varies from Fo_{92} to Fo_{86}, a range which can be accounted for by about 35% fractional crystallisation. The melt inclusions with extreme La/Yb ratios are encircled with a grey outline and the array of melt compositions that can be generated by mixing between these extremes is shown as a grey dotted line. The influence of fractional crystallisation on these melt composition is to cause uniform relative enrichments in La and Yb and the grey shaded field shows the range of melt compositions that can be generated by up to 35% fractional crystallisation of the melts on the binary mixing array.
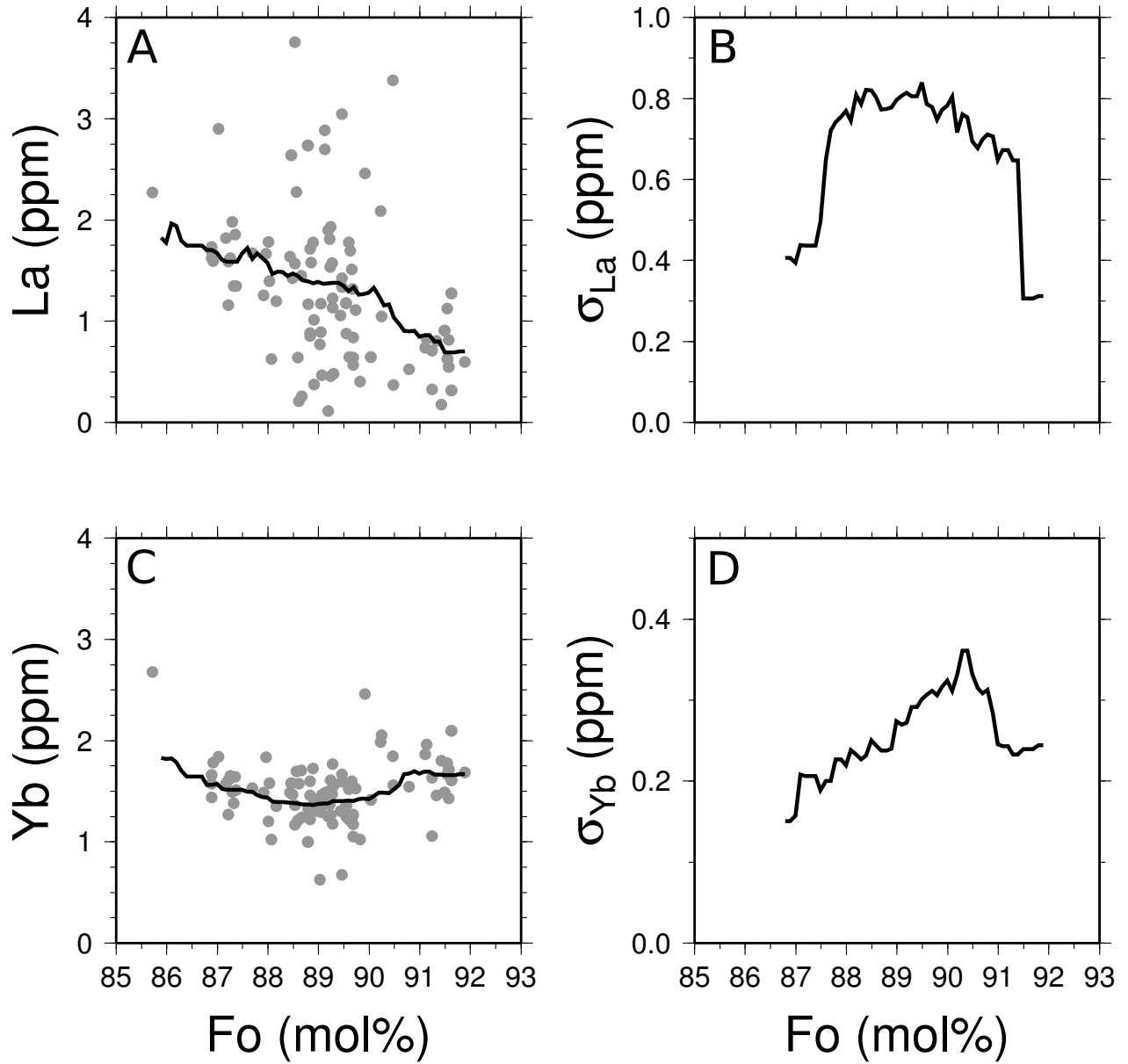
Figure 4: Trace element systematics of olivine-hosted melt inclusions from the Borgarhraun flow in northern Iceland (Maclennan et al., 2003a) plotted against their host olivine compositions. A) La concentrations, with running average calculated using a box-car filter with a full width of 2 mol% forsterite shown as a solid black line. The filtered points are plotted at the mid-point of the window. B) Variation in the standard deviation of the La concentrations, calculated using the same moving window as in A. C) The same as A, but for Yb rather than La. D) The same as B, but for Yb rather than La.
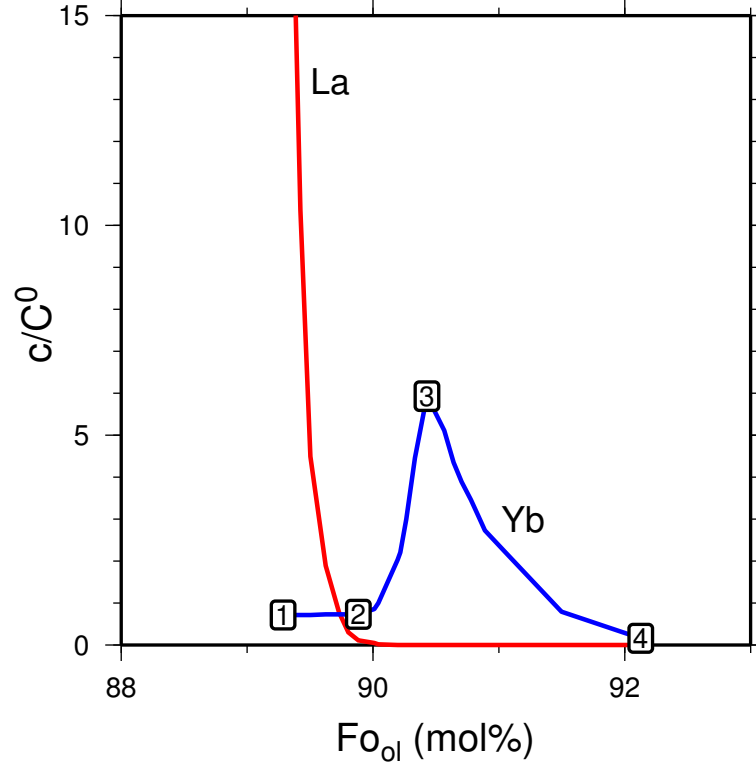
Figure 5: Predictions from the single source peridotite melting model of Maclennan et al. (2003a). The melt compositions are instantaneous fractional melts from a polybaric melting model. The concentrations of La and Yb in the instantaneous fractional melts, c, are provided ratioed to that of their source, C^0, and plotted as a function of the composition of the olivine in equilibrium with these mantle melts. The evolution of La is shown as a red curve and Yb as a blue curve. The numbers on the blue dashed curve show key points in the trace element behaviour that are described in the main text.
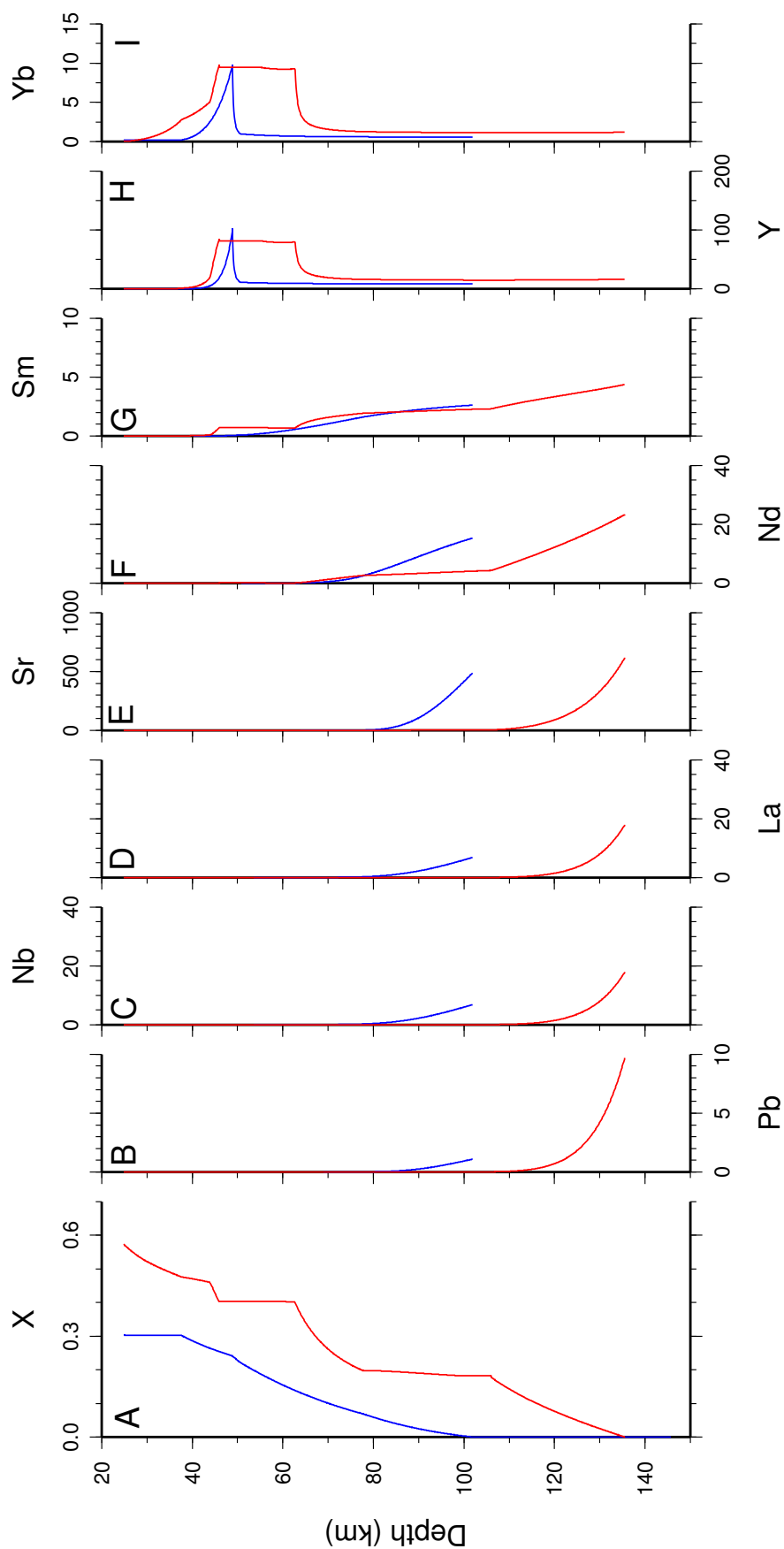
Figure 6: A) Degree of melting as a function of depth for the two lithologies, pyroxenite (red line), and peridotite (blue line). B)-I) Instantaneous fractional melt compositions, in ppm, for a selection of trace elements with varying compatibility. Melts produced from the pyroxenite are shown in red, those from the peridotite are shown in blue.
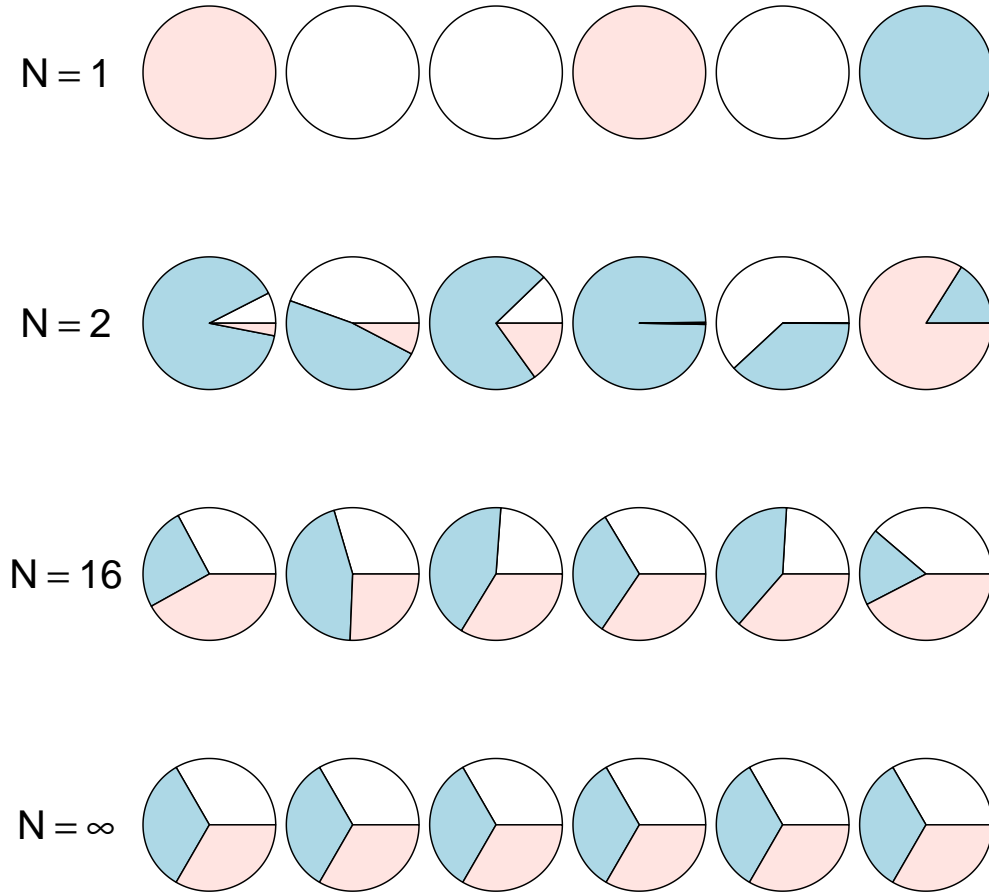
Figure 7: Random samples drawn from a Dirichlet distribution $\mathrm{Dir}\left((N-1)/3, (N-1)/3, (N-1)/3\right)$ shown as pie charts illustrating the behaviour of the mixing parameter N. For illustrative purposes each sample is a mixture of just three possible components (red, blue and white): the true fractional melt population consists of an infinite number of components. The $N=1$ case corresponds to the sampling of the individual components without mixing, and hence each sample is a single colour. The $N=\infty$ case is the well-mixed case where each of the components contributes equally to each sample. The intermediate values of N show variable proportions of each component, becoming more evenly distributed as N increases.
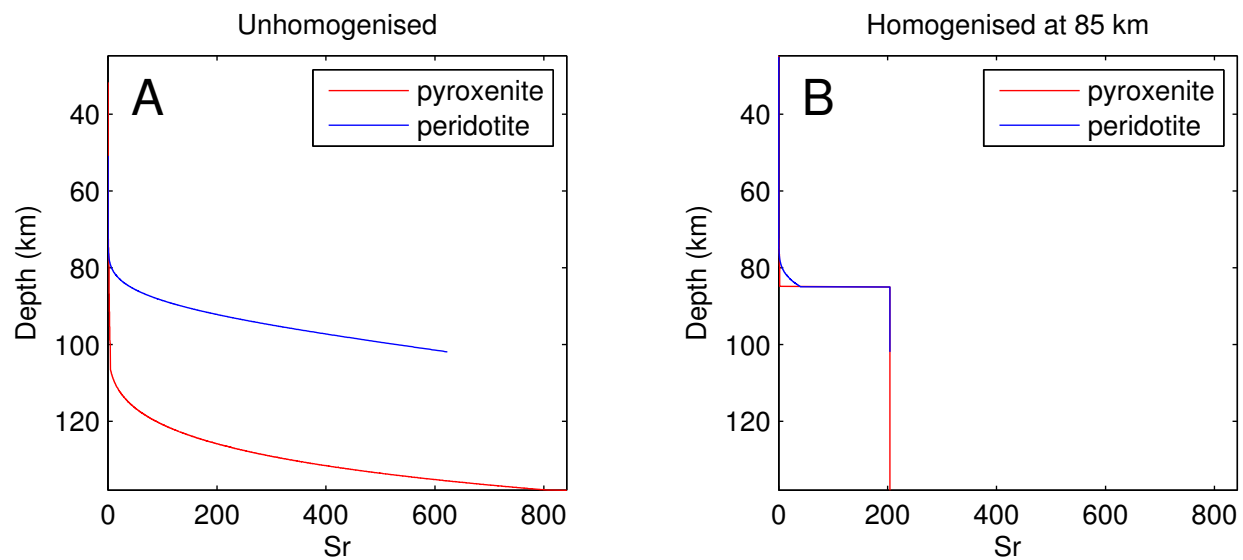
Figure 8: An example of homogenisation at depth. On the left is a plot showing the fractional melt concentration for Sr in ppm as a function of depth. On the right is the same plot, but where all melts below a depth of 85 km have been homogenised over.
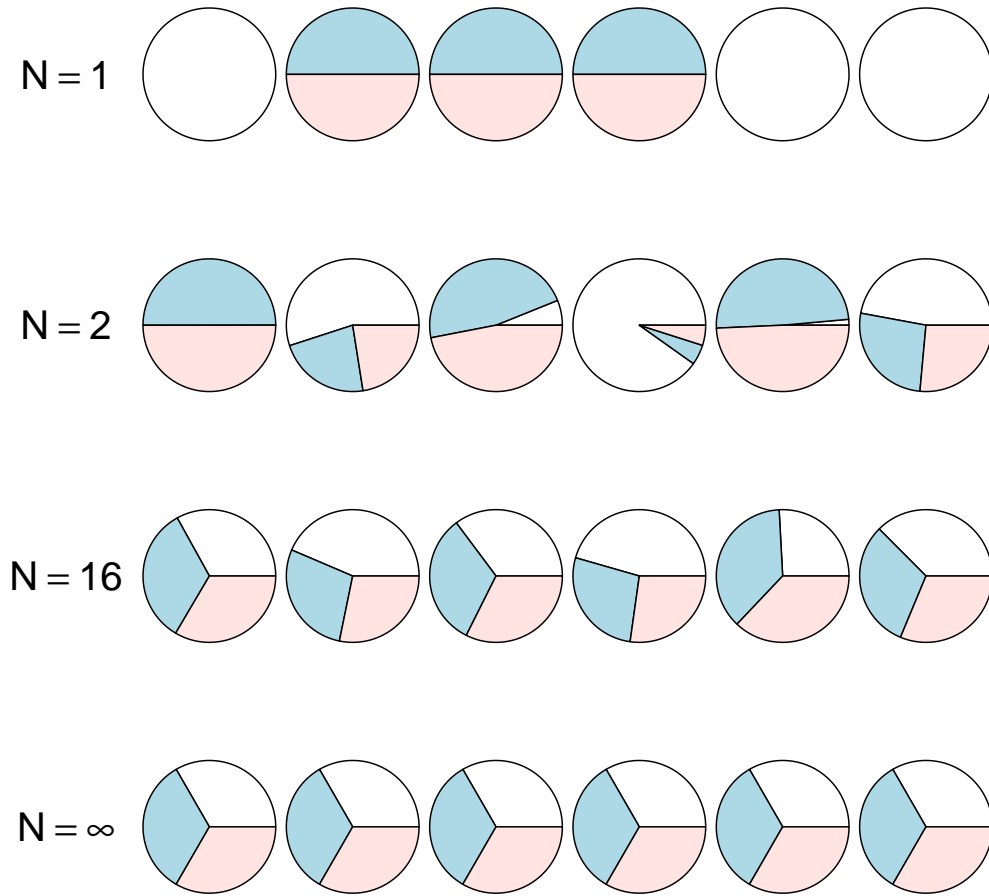
Figure 9: Plot similar to Figure 7 illustrating the effect of homogenisation at depth. In this example, the red and blue components are homogenised over before applying the Dirichlet mixing scheme. They thus occur in equal proportion in every sample, but the relative proportion of the white component to the other two components varies.
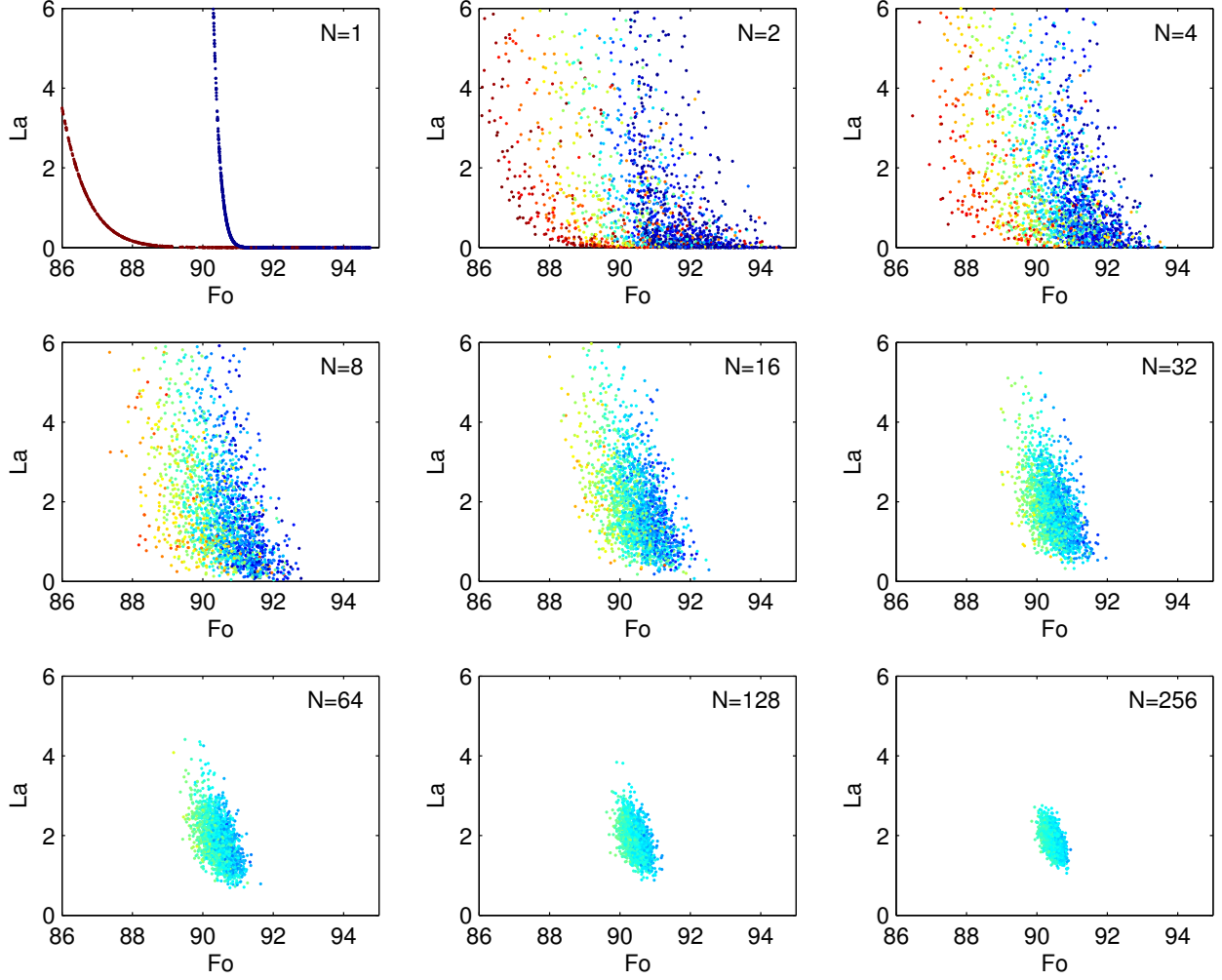
Figure 10: Model run showing La concentration of mixed melts plotted against forsterite content of equilibrium olivine for different values of the mixing parameter N. The top left plot shows $N = 1$, where each sample represents a single fractional melt composition. N then doubles from each plot to the next. The points are coloured according to the proportion (relative mass) in which pyroxenite melting and peridotite melting contribute to the sample: as can be seen in the $N = 1$ plot, dark red corresponds to a melt purely sourced from the pyroxenite; dark blue purely sourced from the peridotite. For large N the data start to resemble an ellipse, as would be expected from the central limit theorem.
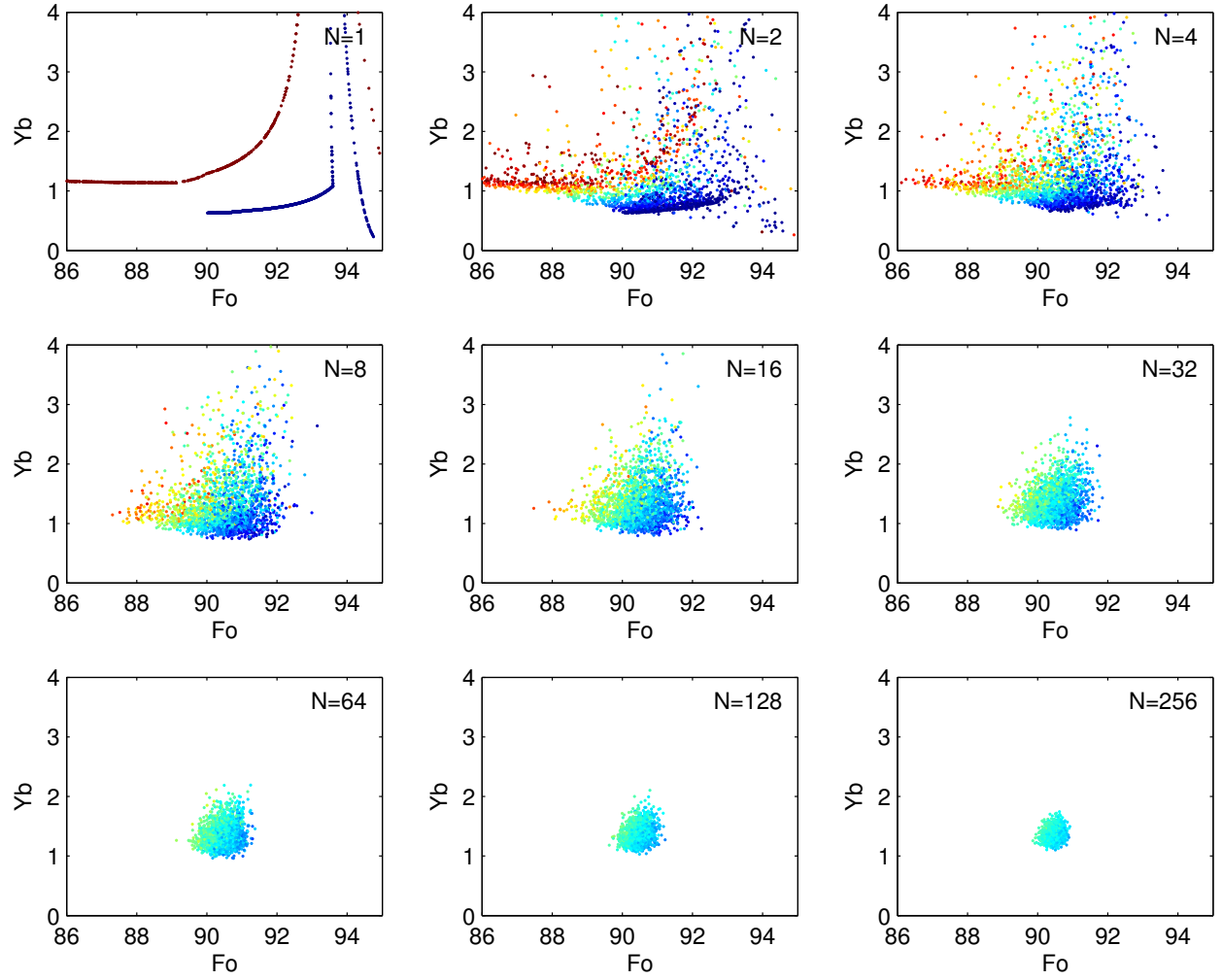
Figure 11: Model run as in Figure 10, with Yb concentration of mixed melts plotted against forsterite content of the equilibrium olivine. Notice the small range in Yb concentrations in the fractional melts ($N = 1$) compared with the steep fractional melt curves for the highly incompatible La in Figure 10.
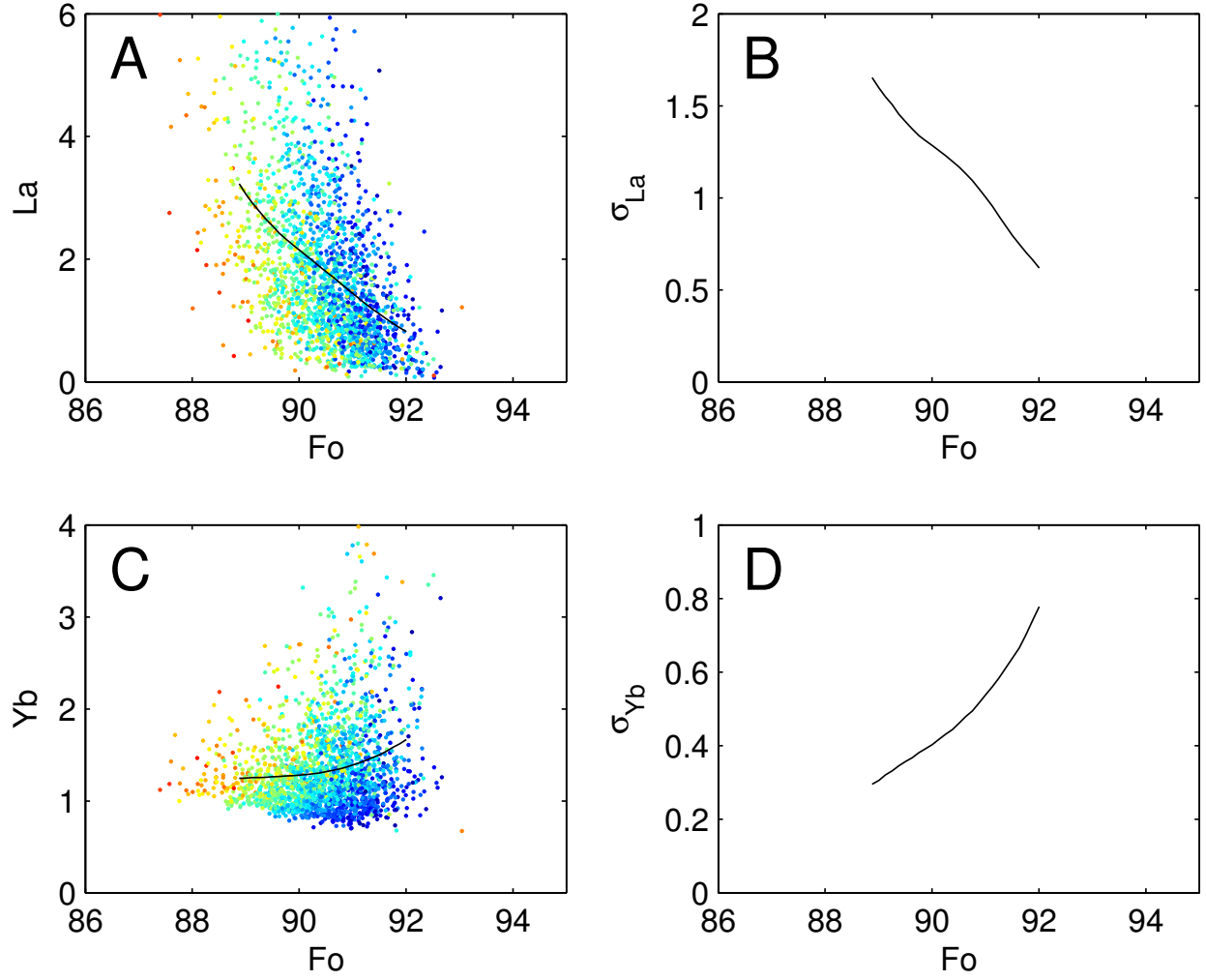
Figure 12: Model run with $N = 12$. The plots on the left hand side (A and C) show La and Yb concentrations of mixed melts against the forsterite content of the equilibrium olivine, similar to the plots in Figures 10 and 11. The black lines on these plots show a running mean of the La and Yb concentrations for fixed forsterite content (using a window width of 1 Fo unit). The plots on the right hand side (B and D) show the standard deviations of the La and Yb concentrations at fixed forsterite content (again using a window width of 1 Fo unit). Notice that the La standard deviation increases substantially with decreasing Fo content, whereas the Yb standard deviation does the opposite. These plots should be compared with those of Figure 4 for the Borgarhraun melt inclusion data.
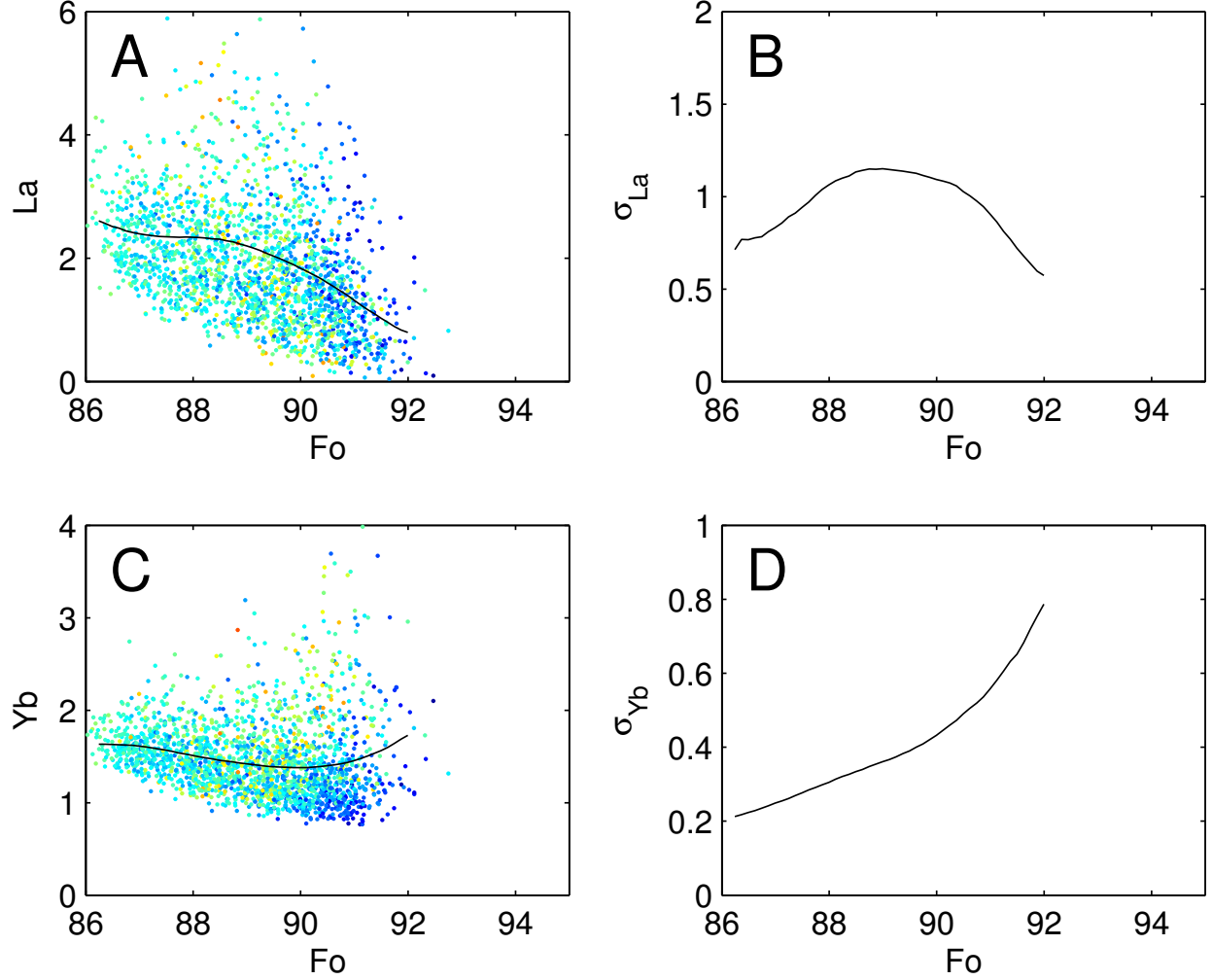
Figure 13: Model run similar to that in Figure 12, but with the inclusion of fractional crystallisation and concurrent mixing. Each sample undergoes fractional crystallisation with a range from 0 to 20%. The mixing parameter N is a function of this degree of crystallisation and varies from $N = 12$ with no crystallisation to $N = 108$ at 20% crystallisation. The key effects of this concurrent mixing and fractionation is to allow the Fo number to range to lower values (as a result of the crystallisation) and to reduce the variance in trace element concentrations at low Fo numbers (as a result of the mixing). Notice that the patterns are now more similar to that seen in Figure 4 for the Borgarhraun melt inclusion data: the standard deviation of La concentration increases with decreasing Fo number up to a peak around Fo=88 and then decreases for further decreases in Fo number. The standard deviation of Yb concentration simply shows a monotonic decrease with decreasing Fo number.
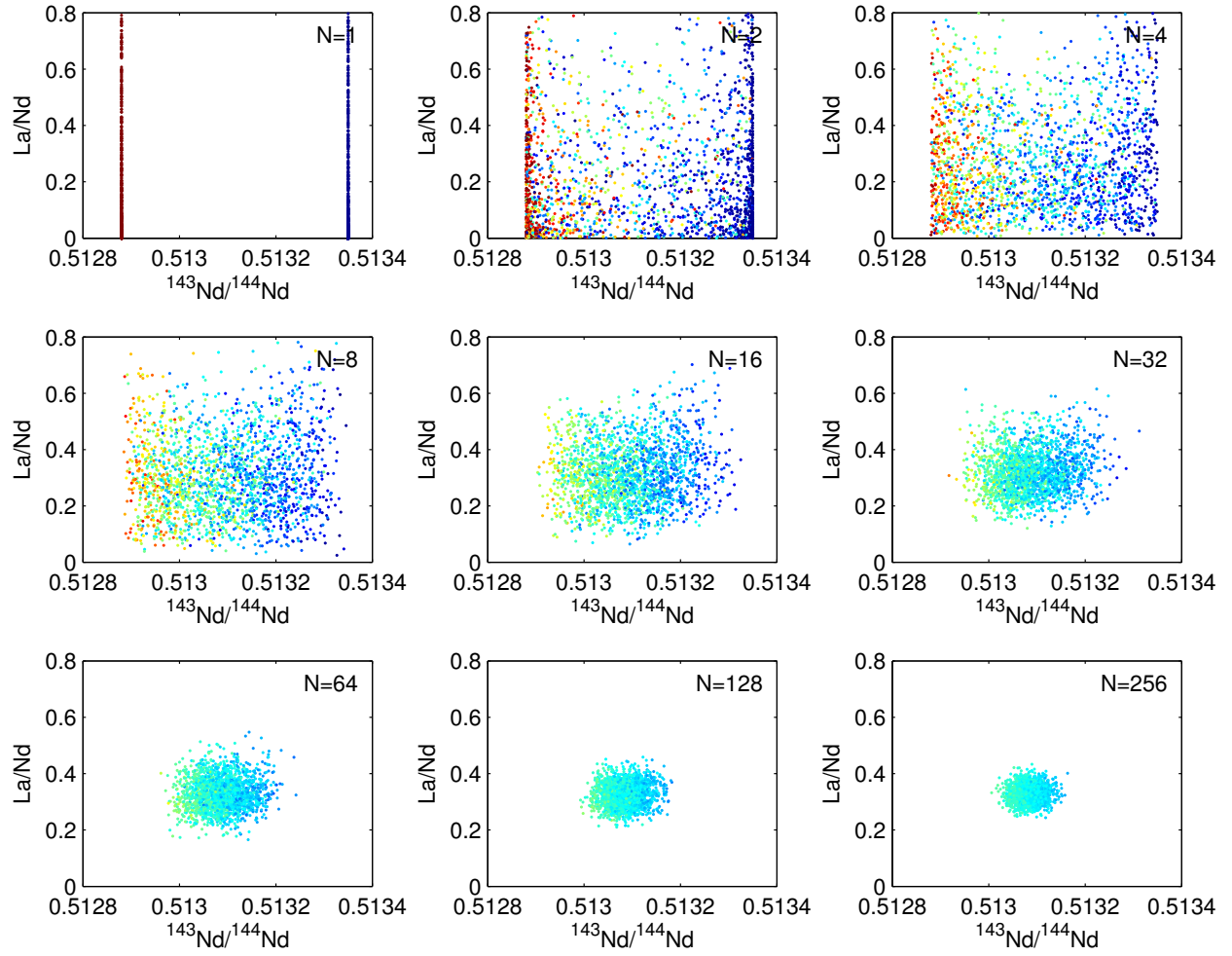
Figure 14: Model run showing La/Nd against ^{143}Nd/^{144}Nd for different values of the mixing parameter N. Note that there is little correlation between La/Nd and ^{143}Nd/^{144}Nd.
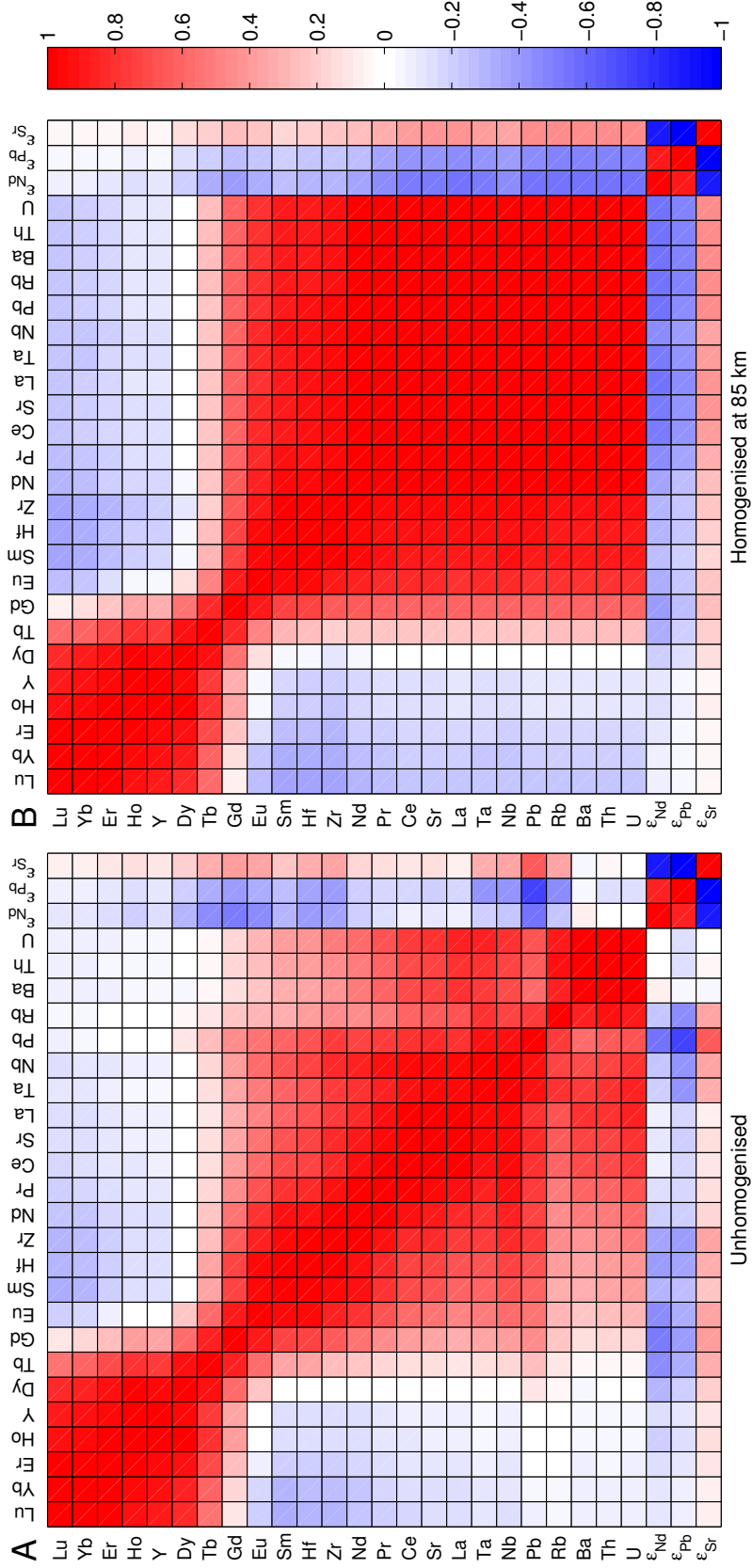
Figure 15: Correlation matrix plots for model runs without homogenisation at depth (A) and with homogenisation at a depth of 85 km (B). Dark red indicates perfect positive correlation ($r = 1$), white no correlation ($r = 0$), and dark blue perfect negative correlation ($r = -1$). For the trace elements the correlation matrix is independent of the mixing parameter N; for the isotopic ratios there is a dependence on N: the plots above are for $N = \infty$. As would be expected, elements with similar compatibilities correlate well. Homogenisation at depth improves the correlations amongst the most incompatible elements (Hf to U). The expressions for calculating these correlation coefficients can be found in Appendix C.
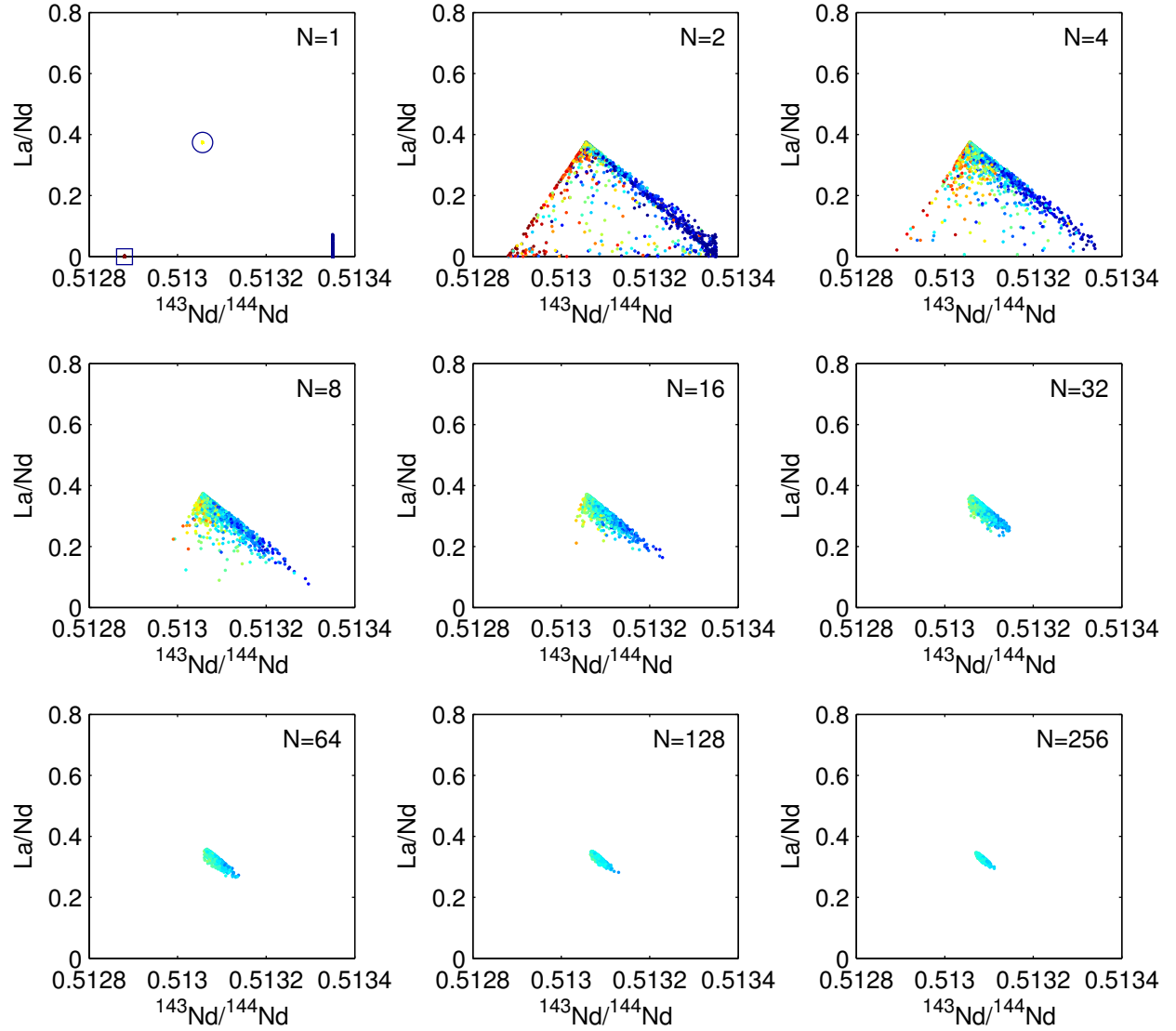
Figure 16: Model run showing La/Nd against ^{143}Nd/^{144}Nd as in Figure 14, except now all melts below a depth of 85 km are homogenised over. The composition of the homogenised deep melts is indicated by a circle in the $N = 1$ plot, and the composition of the unhomogenised shallow melts of the pyroxenite by a square. Notice that for large N there is a strong inverse correlation between La/Nd and ^{143}Nd/^{144}Nd (where there was little correlation in Figure 14).
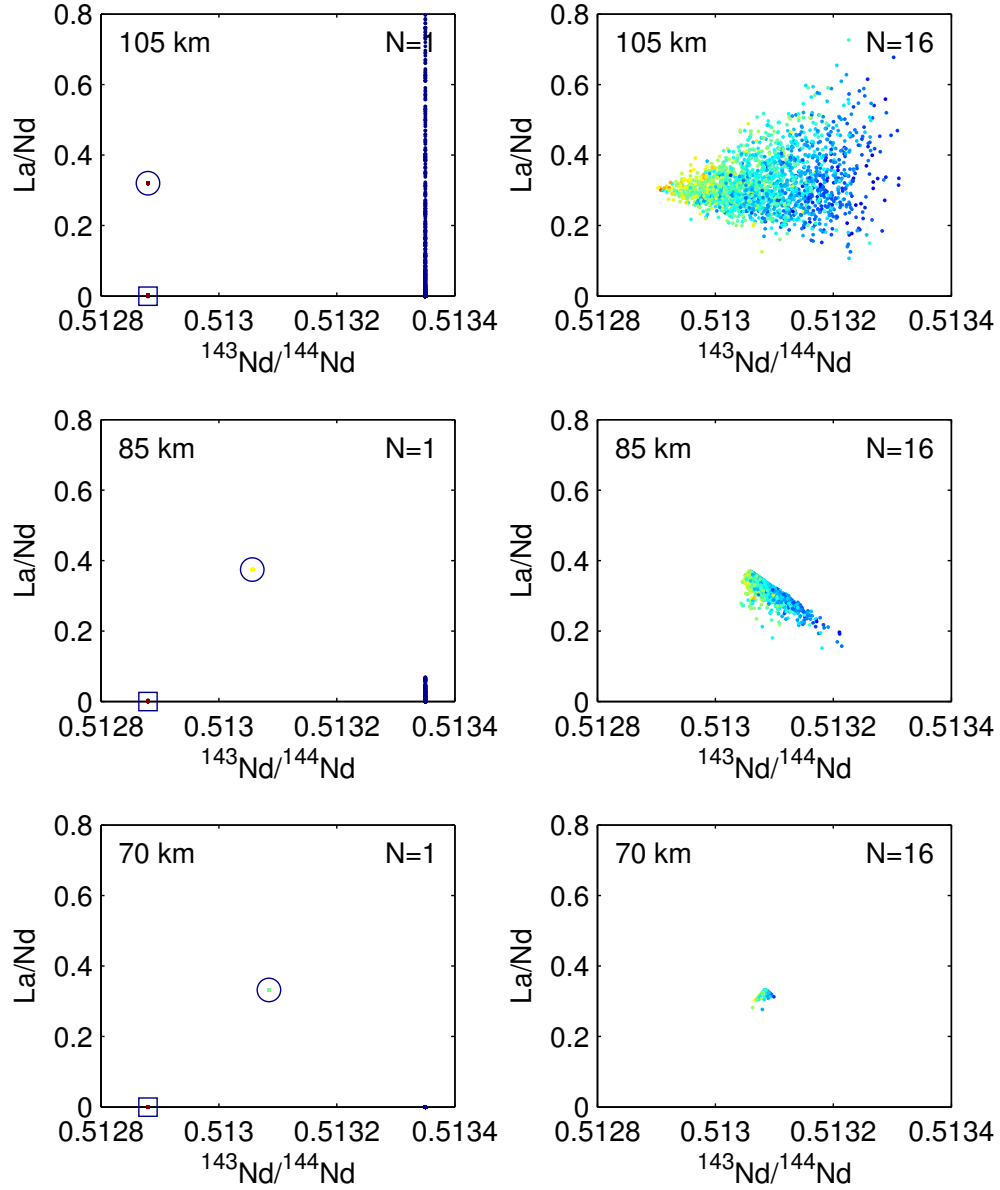
Figure 17: Model run showing La/Nd against ^{143}Nd/^{144}Nd as in Figures 14 and 16, demonstrating the effect of varying the homogenisation depth. Each subplot is labelled with homogenisation depth in the top left and N in the top right. The composition of the homogenised deep melts is indicated by a circle in the $N = 1$ subplots, and the composition of the unhomogenised shallow melts of the pyroxenite by a square. The middle panels are for a homogenisation depth of 85 km as in Figure 16. The top panels are for a deeper homogenisation depth of 105 km (just before the onset of peridotite melting, see Figure 6A). The bottom panels are for a shallower homogenisation depth of 70 km at which point there has been significant peridotite melting (around 10%, see Figure 6A)
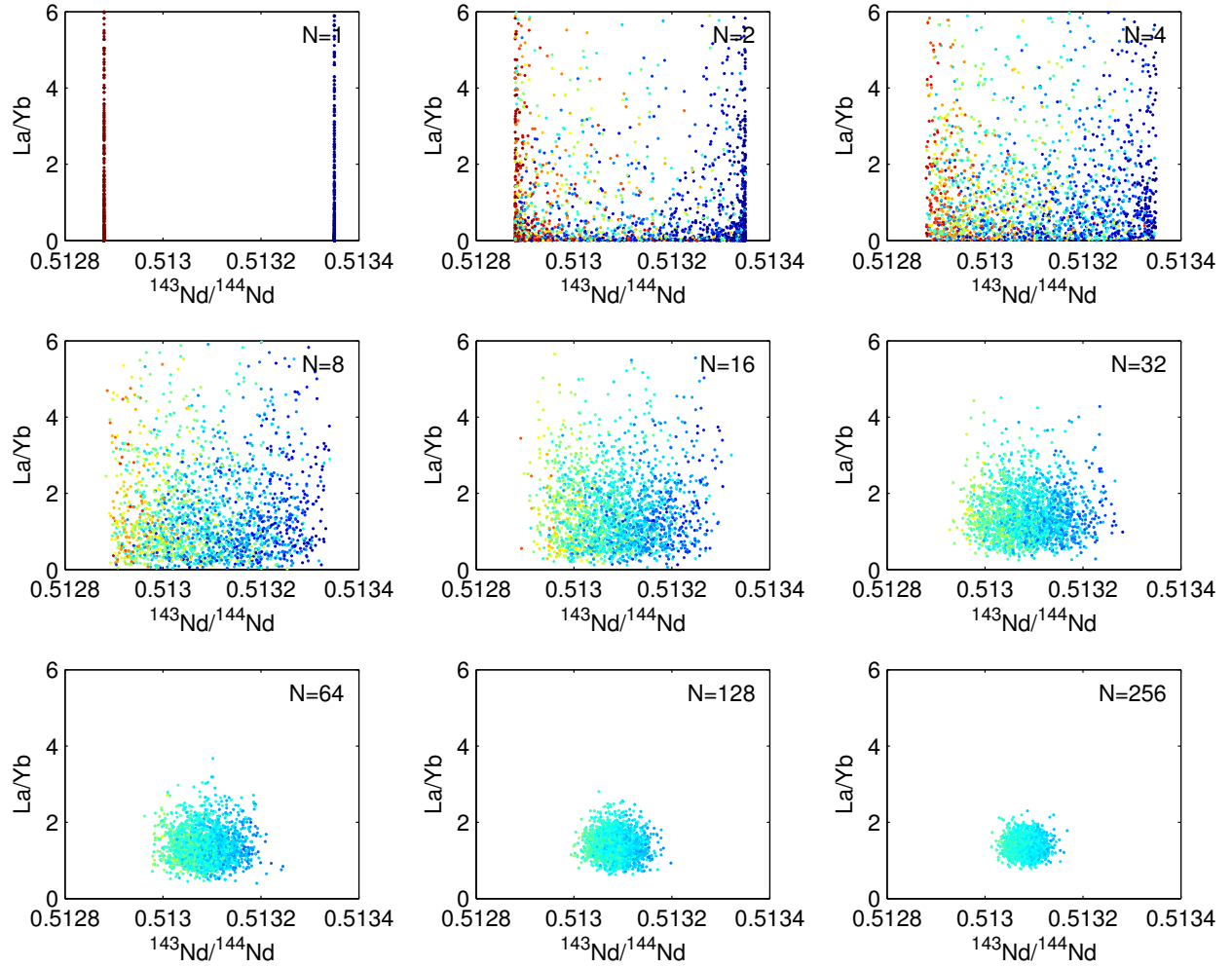
Figure 18: Model run showing La/Yb against ^{143}Nd/^{144}Nd for different values of the mixing parameter N. Note that there is little correlation between La/Yb and ^{143}Nd/^{144}Nd.

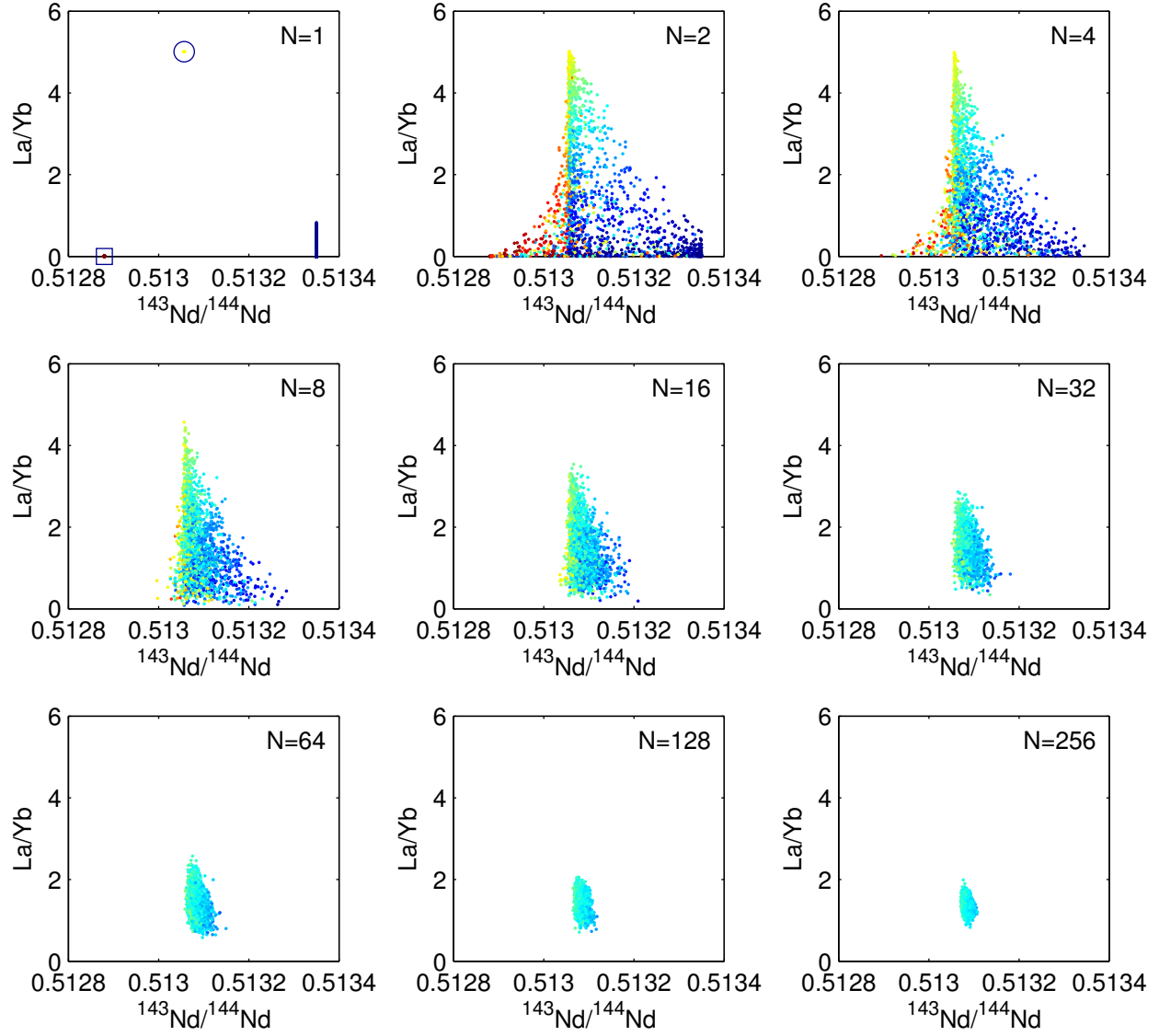Figure 19: Model run showing La/Yb against ^{143}Nd/^{144}Nd as in Figure 18, except now all melts below a depth of 85 km are homogenised over. For $N \geq 16$ there is distinctive pattern to the data with a greater variance in La/Yb at low ^{143}Nd/^{144}Nd than at high ^{143}Nd/^{144}Nd. Moreover the highest ^{143}Nd/^{144}Nd corresponds to the lowest La/Yb. This distinctive pattern can be contrasted with the more circular patterns seen without the homogenisation at depth in Figure 18.
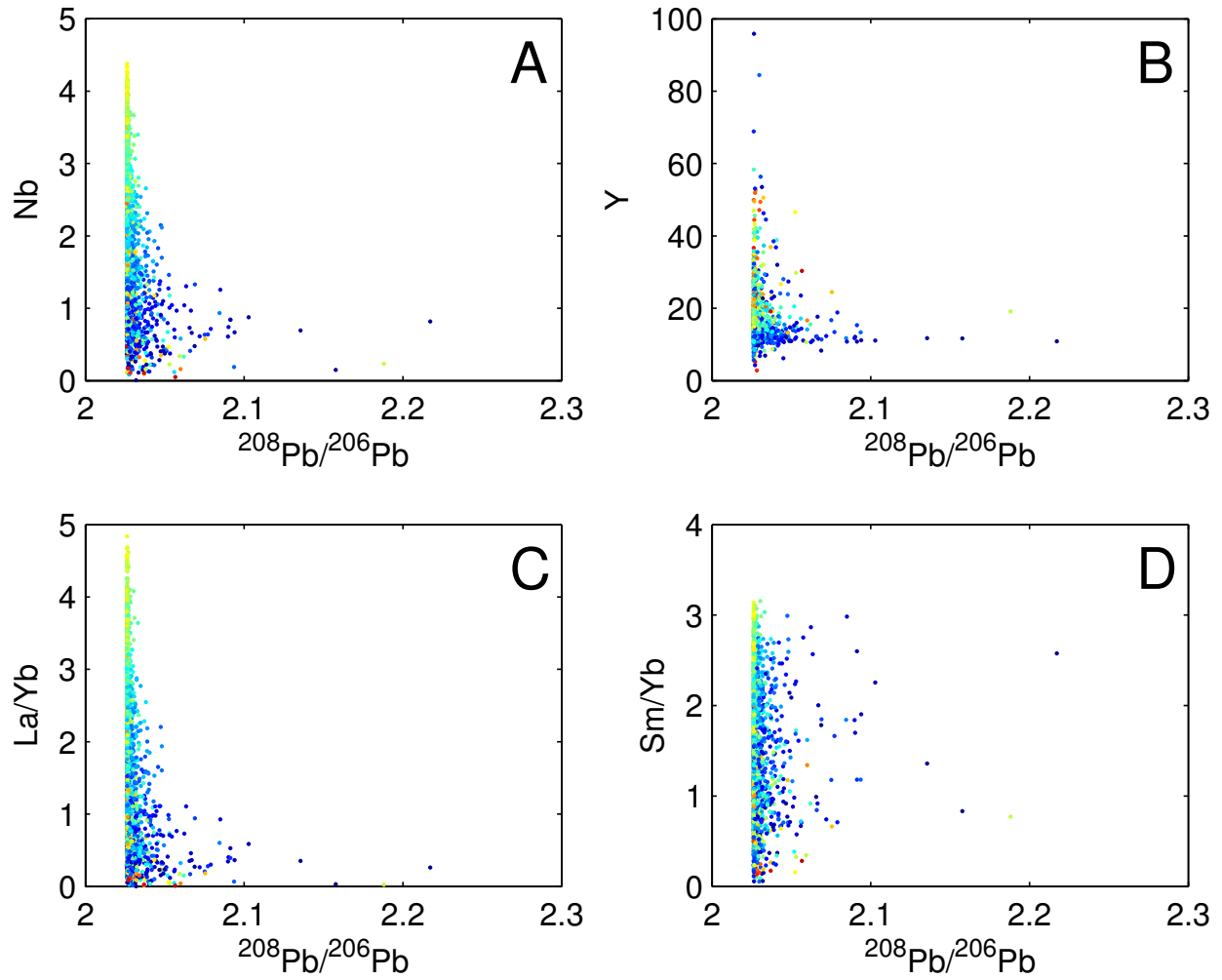
Figure 20: Model run with $N = 5$ and a homogenisation depth of 85 km. Nb, Y, La/Yb and Sm/Yb are plotted against ^{208}Pb/^{206}Pb. Some similarities can be seen with the patterns in the whole rock and melt inclusion data plotted in Figure 1. At low ^{208}Pb/^{206}Pb there is a large variance in Nb and Y concentrations, with the variance reducing as ^{208}Pb/^{206}Pb increases. High ^{208}Pb/^{206}Pb corresponds to low Nb concentrations. The sources have isotopic ratios ^{208}Pb/^{206}Pb=1.99 (pyroxenite) and 2.28 (peridotite).
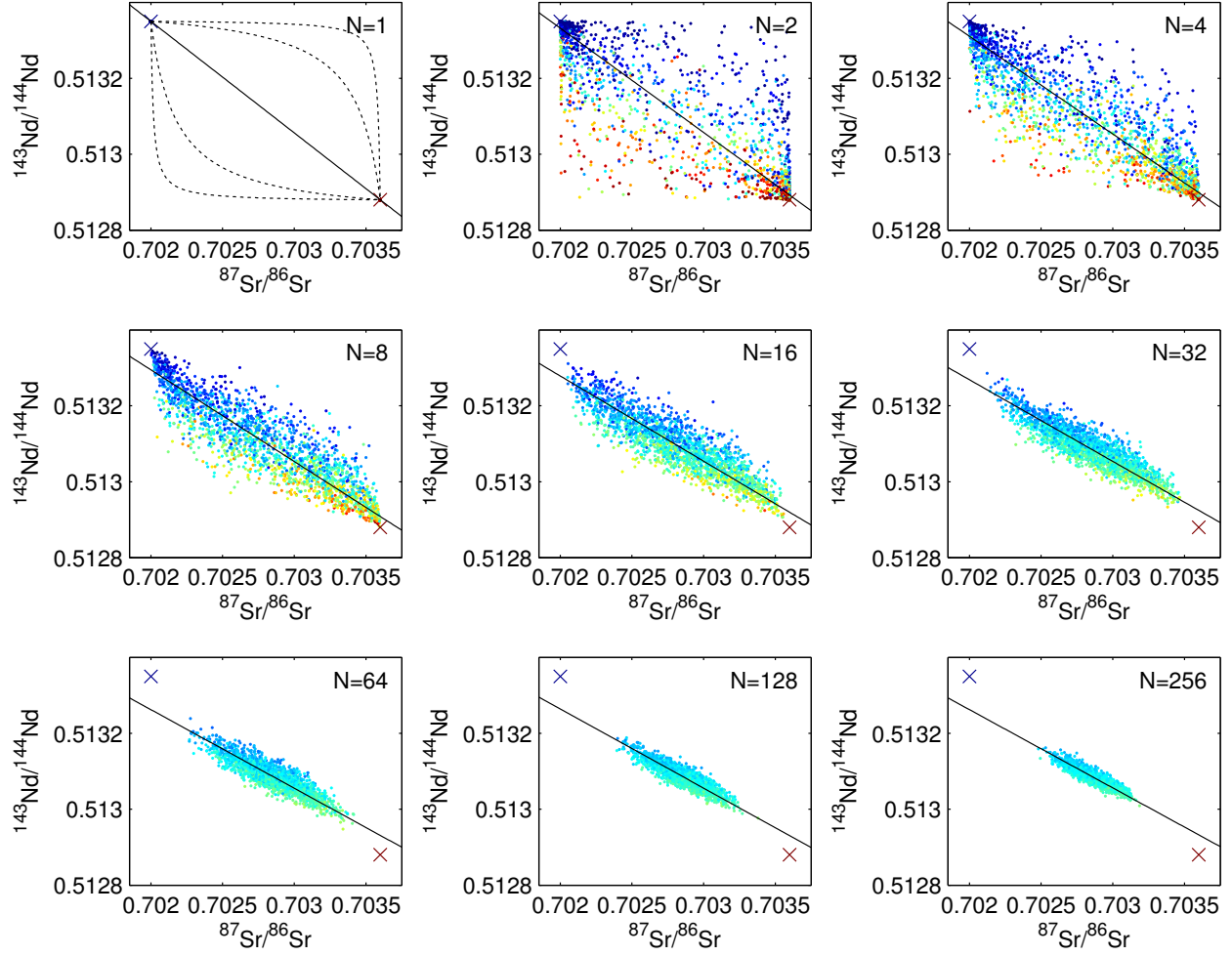
Figure 21: Model run showing ^{143}Nd/^{144}Nd plotted against ^{87}Sr/^{86}Sr for different values of the mixing parameter N. Colour coding is as in Figures 10 and 11. Crosses show the isotopic compositions of the peridotite and pyroxenite sources. The black line in each plot is a best fit regression line through the data. Notice that the regression lines do not go through the isotopic compositions of the sources, except when $N = 1$. When $N = 1$ it is only possible to get isotopic ratios identical to that of the two source (the crosses). For comparison, a series of binary mixing curves are shown in the $N = 1$ subplot, with ratio of concentration ratios $\gamma = 0.01, 0.1, 1, 10, 100$.
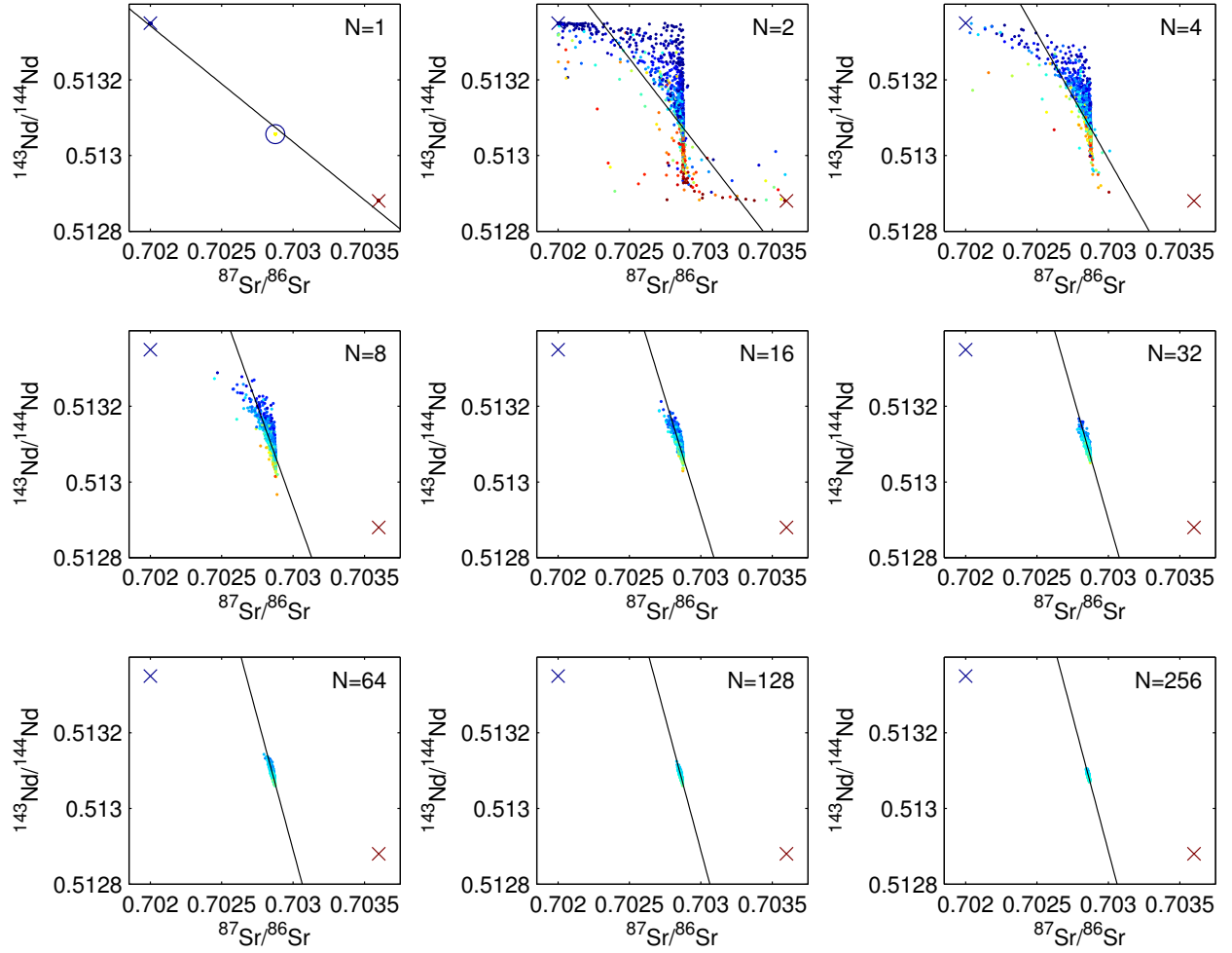
Figure 22: Model run showing ^{143}Nd/^{144}Nd plotted against ^{87}Sr/^{86}Sr as in Figure 21, except now all melts below a depth of 85 km are homogenised over. The composition of the homogenised deep melts is indicated by a circle in the $N = 1$ plot. As in Figure 21, the regression lines do not go through the isotopic compositions of the sources, and moreover the slopes of the regression lines have changed substantially.
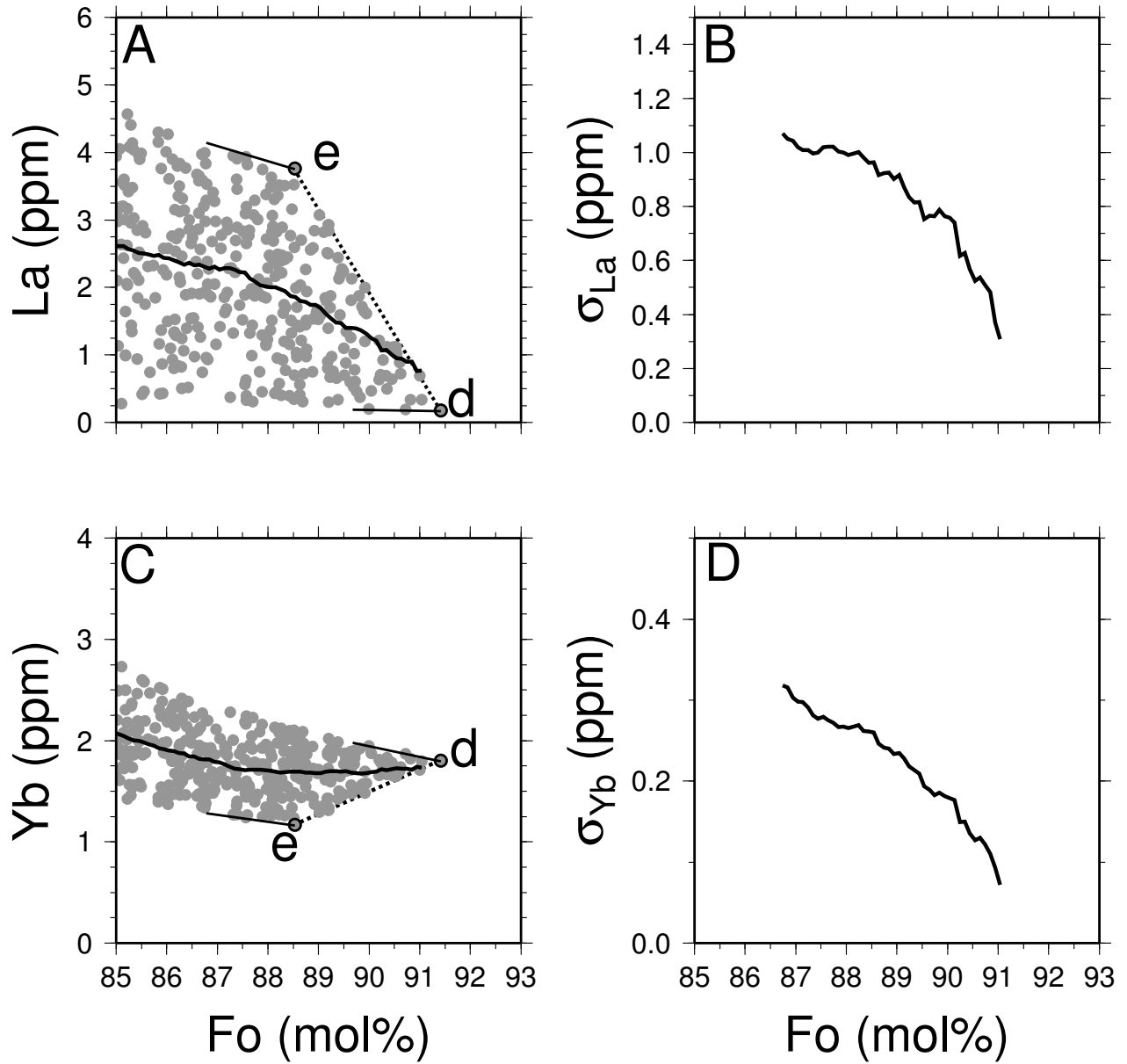
Figure 23: Trace element systematics of synthetic dataset of melt composition produced by variable extents of binary mixing of two melts followed by variable extents of fractional crystallisation. The plots are the same as for Figure 4 with the addition of the compositions of the melt inclusions used as end-member melts. The depleted end-member is labelled 'd' and the enriched one is labelled 'e' and the dotted lines on A and C shows the predicted array of melts and olivine hosts that can be generated by variable extents of mixing of these end-members. The predicted compositions generated after 10% crystallisation of the end-members are shown as thin black lines on A and C.
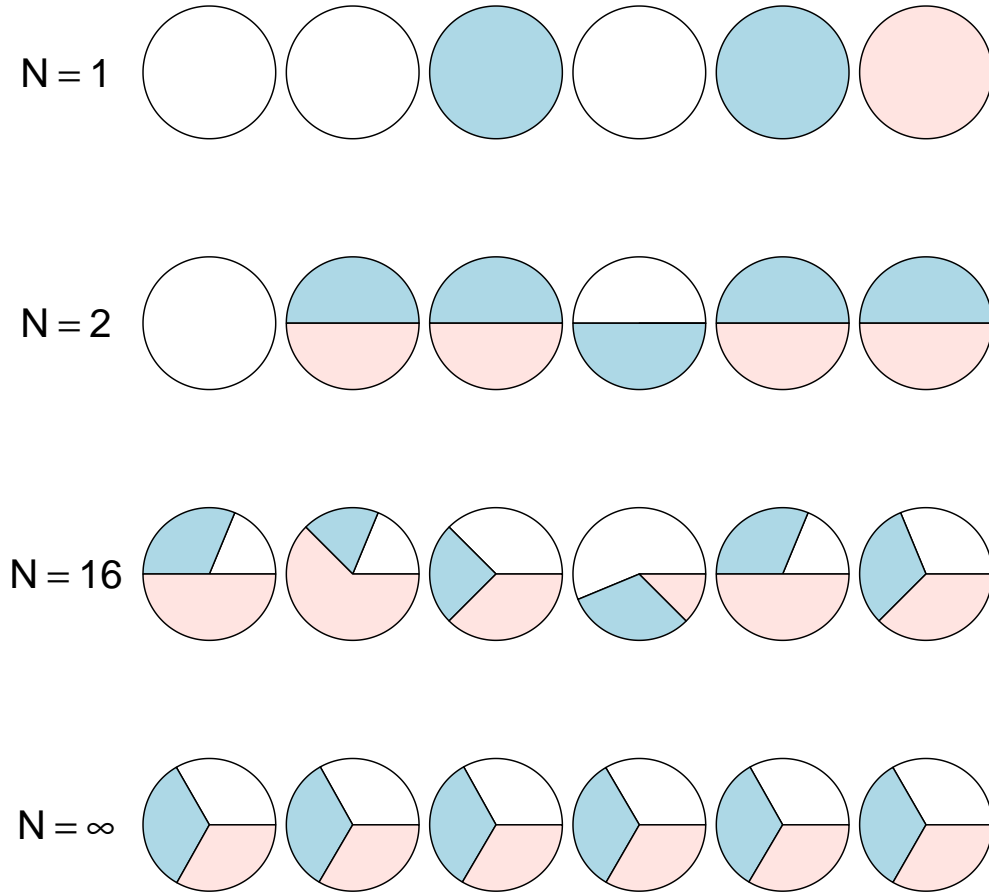
Figure 24: An illustration of the discrete mixing scheme used by Rudge et al. (2005) to be compared with the continuous Dirichlet mixing scheme used in this work. As in Figure 7, the underlying distribution is taken to have just three components for illustrative purposes. The relative mixing proportions have a Multinomial $(N, [1/3, 1/3, 1/3])$ distribution. The discrete nature of this scheme is particularly notable for the case of $N = 2$, where each sample must be a 50-50 mixture of the 3 possible components.